J. Fluid Mech. (2021), *vol*. 928, A14, doi:10.1017/jfm.2021.793

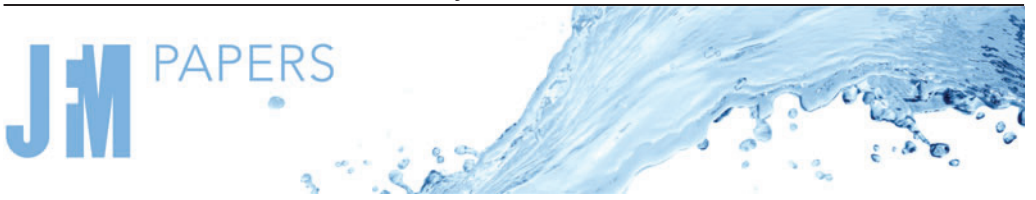

Diffusive effects in local instabilities of a baroclinic axisymmetric vortex

Suraj Singh[1],† **and Manikandan Mathur**[1],†

[1]Department of Aerospace Engineering & Geophysical Flows Lab, Indian Institute of Technology Madras, Chennai 600036, India

(Received 13 February 2021; revised 15 July 2021; accepted 27 August 2021)

We present a local stability analysis of an idealized model of the stratified vortices that appear in geophysical settings. The base flow comprises an axisymmetric vortex with background rotation and an out-of-plane stable stratification, and a radial stratification in the thermal wind balance with the out-of-plane momentum gradient. Solving the local stability equations along fluid particle trajectories in the base flow, the dependence of short-wavelength instabilities on the Schmidt number Sc (ratio between momentum and mass diffusivities) is studied, in the presence of curvature effects. In the diffusion-free limit, the well-known symmetric instability is recovered. In the viscous, double-diffusive regime, instability characteristics are shown to depend on three non-dimensional parameters (including Sc), and two different instabilities are identified: (i) a monotonic instability (same as symmetric instability at $Sc = 1$), and (ii) an oscillatory instability (absent at $Sc = 1$). Separating the base flow and perturbation characteristics, two each of base flow and perturbation parameters (apart from Sc) are identified, and the entire parameter space is explored for the aforementioned instabilities. In comparison with $Sc = 1$, monotonic and oscillatory instabilities are shown to significantly expand the instability region in the space of base flow parameters as Sc moves away from unity. Neutral stability boundaries on the plane of Sc and a modified gradient Richardson number are then identified for both these instabilities. In the absence of curvature effects, our results are shown to be consistent with previous studies based on normal mode analysis, thus establishing that the local stability approach is well suited to capturing symmetric and double-diffusive instabilities. The paper concludes with a discussion of curvature effects, and the likelihood of monotonic and oscillatory instabilities in typical oceanic settings.

Key words: baroclinic flows, rotating flows, vortex instability

† Email addresses for correspondence: surajsingh108talk@gmail.com, manims@ae.iitm.ac.in

1. Introduction

Eddies, along with fronts, i.e. regions of relatively sharp horizontal density gradients, are common occurrences in the atmosphere and the ocean. In the atmosphere, baroclinic and barotropic instabilities result in the formation of cyclones and anticyclones (Emanuel, Fantini & Thorpe 1987), and the resulting advection of temperature leads to the formation of fronts (Hoskins & Bretherton 1972). Similar processes occur in the ocean too. For example, tropical instability near the equator can result in the formation of tropical instability vortices which are associated with strong equatorial sea surface temperature fronts (Holmes *et al.* 2014). Alternatively, processes such as wind and topographical variations can lead to the development of submesoscale eddies such as the structures which are associated with frontal regions (Mahadevan 2006). In addition, stirring by mesoscale (around 100 km or more, corresponding to a Rossby number much smaller than unity) and submesoscale (1–100 km, corresponding to a Rossby number around unity) eddies can form frontal regions too (Shcherbina *et al.* 2015; Sarkar *et al.* 2016). The dynamics of these eddies, apart from significantly influencing the transport of various quantities such as heat, salinity and nutrients (Zhang, Wang & Qiu 2014), can also have significant implications for large-scale phenomena like the El Niño southern oscillation and the equatorial heat budget (Holmes *et al.* 2014). Furthermore, the dynamics of submesoscale coherent vortices is an important consideration to understand transport and mixing in many parts of the ocean (McWilliams 1985).

Large-scale geophysical eddies, apart from their vortical structure, often have a vertical (out of plane) gradient of momentum which is in thermal wind balance with the horizontal density variation (Pedlosky 1987). Factors such as background rotation and vertical stratification also affect the dynamics of these vortices. In addition, curvature effects have also been shown to have an effect on frontogenesis and the adjustment of fronts near vortices (Shakespeare 2016). Instabilities in these vortices represent an important pathway towards small-scale turbulence and mixing (Thomas, Tandon & Mahadevan 2008), thus playing a key role in parameterization of small-scale processes in large-scale climate models (Fox-Kemper, Ferrari & Hallberg 2008; Bachman *et al.* 2017). In addition, their instability characteristics can also help in interpreting field observations (Ruddick 1992; D'Asaro *et al.* 2011; Thompson *et al.* 2016) and large-scale climate model outputs (Fox-Kemper *et al.* 2011), which in turn motivate fine-scale process studies (Mahadevan & Tandon 2006).

Instabilities in geophysical vortices could range from purely inertial, such as the centrifugal instability in unstratified planar vortices (Kloosterziel & Van Heijst 1991), to purely convective, resulting from statically unstable vertical stratification (Chandrasekhar 1961). The intermediate regimes, where both inertial and buoyancy effects are present, can be conducive to what is called the symmetric instability (Hoskins 1974; Xui & Clark 1985; Thomas *et al.* 2013). Purely centrifugal instabilities are generally suppressed by Coriolis forces (Godeferd, Cambon & Leblanc 2001) but could play an important role in regions with anticyclonic vorticity and near the equator, where Rossby numbers are near unity (Haine & Marshall 1998). Symmetric instability can result in slantwise convection along tilted constant angular momentum surfaces when the potential vorticity is negative in an inviscid, adiabatic environment (Hoskins 1974). Recently, curvature effects on the symmetric instability have been studied, and their importance in oceanic eddies has been highlighted (Buckingham, Gula & Carton 2021*a*,*b*). In addition, hyperbolic instabilities could also manifest in regions of high strain near the edges of vortices with hyperbolic stagnation points (Leblanc 1997). Apart from the aforementioned local instabilities, global instabilities such as the Kelvin–Helmholtz (Peltier & Caulfield 2003) and baroclinic instabilities (Pierrehumbert & Swanson 1995) are also a consideration in stratified eddies.

Vortices in thermal wind balance can also become unstable due to unequal mass and momentum diffusivities. McIntyre (1970), using normal mode theory in a locally Cartesian region of an eddy in thermal wind balance, showed that a Prandtl number away from unity modifies the symmetric instability criterion, and also introduces a local oscillatory instability. Laboratory experiments have demonstrated the occurrence of such an oscillatory instability, and resulting density layers (Baker 1971; Meunier *et al.* 2014). Studies regarding instabilities in long-lived mesoscale oceanic eddies have considered this diffusive instability mechanism to explain intrusions found in density profiles (Ruddick 1992; Kuzmina & Zhurbas 2000). Experimental studies have also observed the formation of density layers at a Prandtl number less than unity, which was further suggested to explain the layers on the scale of 1 m seen in certain parts of the ocean. (Calman 1977; Weber 1980). An energetics-based approach to derive the results of McIntyre (1970) in a parallel shear flow was presented by Kloosterziel & Carnevale (2007). Here, we use the local stability approach (Lifschitz & Hameiri 1991) with small diffusivities in momentum and density to investigate short-wavelength instabilities in stratified eddies in thermal wind balance. Previous studies using the local stability approach have captured the effects of differential diffusion (in mass and momentum) on local instabilities in radially stratified circular Couette flow (Kirillov & Mutabazi 2017) and vertically stratified planar vortices (Singh & Mathur 2019).

In this study, we explore local instabilities in horizontally and vertically stratified vortices in thermal wind balance, including the effects of differential diffusion in mass and momentum. The local stability approach is first demonstrated to be efficient in capturing symmetric and double-diffusive instabilities. Apart from being based on a different approach compared with McIntyre (1970), our study is also wider in scope compared with that of McIntyre (1970) in three significant aspects: (i) exploration in the centrifugally unstable regime, (ii) viscous instability characteristics away from the neutral stability boundaries in both the centrifugally stable and unstable regimes and (iii) curvature effects. The local stability framework and the base flow configuration are described in § 2 followed by our results on the instability characteristics in § 3. The importance of our results, particularly the curvature effects, are discussed in three different contexts in § 4, following which the conclusions are presented in § 5.

2. Theory

The governing equations of motion for an incompressible flow with background rotation $\Omega \boldsymbol{e}_z$ ($\boldsymbol{e}_z$ is the unit vector along the positive z-axis), within the Boussinesq approximation, are

$$\boldsymbol{\nabla} \cdot \boldsymbol{u} = 0, \tag{2.1}$$

$$\frac{\mathrm{D}\boldsymbol{u}}{\mathrm{D}t} + 2\Omega \boldsymbol{e}_z \times \boldsymbol{u} = -\frac{\boldsymbol{\nabla} p}{\rho_0} - g\frac{\rho}{\rho_0}\boldsymbol{e}_z + \nu \nabla^2 \boldsymbol{u}, \tag{2.2}$$

$$\frac{\mathrm{D}\rho}{\mathrm{D}t} = \kappa \nabla^2 \rho, \tag{2.3}$$

where t is time, ρ, $\boldsymbol{u}$ and p the density, velocity and pressure, respectively, and gravity $\boldsymbol{g} = -g\boldsymbol{e}_z$ with $g > 0$; ρ_0, ν and κ are the reference density, kinematic viscosity and diffusion coefficient associated with density, respectively.

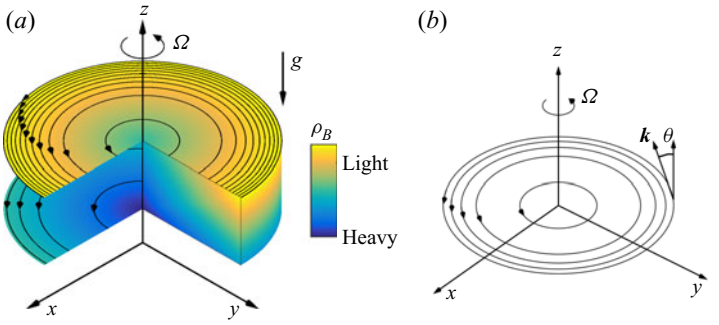

Figure 1. (*a*) A schematic of the axisymmetric base flow ($\boldsymbol{u_B} = V(r, z)\boldsymbol{e_\omega}$) considered in this study. The colour indicates density, and the black curves denote streamlines. The radial spacing between neighbouring streamlines is inversely proportional to the magnitude of the local azimuthal velocity. The flow is stably stratified along z. The radial density gradient and the vertical (along z) gradient of the azimuthal velocity are in thermal wind balance (2.5). (*b*) Schematic showing the perturbation wave vector $\boldsymbol{k}$ and the angle θ it makes with the z-axis.

2.1. *Base flow*

We consider a base flow field that describes an axisymmetric vortex in stratified surroundings. Specifically, the velocity field is given by

$$\boldsymbol{u}_B = V(r, z)\boldsymbol{e}_\omega, \tag{2.4}$$

where (r, ω, z) represent the cylindrical polar coordinates, and the subscript B denotes base flow quantities. The corresponding density field is given by $\rho_B(r, z)$, with its vertical and radial gradients characterized by the Brunt Väisälä frequency $N_z = \sqrt{-(\partial\rho_B/\partial z)(g/\rho_0)}$ ($N_z^2 > 0$ throughout the current study), and $N_r = \sqrt{-(\partial\rho_B/\partial r)(g/\rho_0)}$. Finally, the pressure associated with the base flow is denoted as $p_B(r, z)$. The base flow field satisfies the mass conservation (2.1), the azimuthal component of the inviscid momentum equation ((2.2) with $\nu = 0$) and the diffusion-free incompressibility condition ((2.3) with $\kappa = 0$). Furthermore, requiring the base flow to satisfy the radial component of (2.2) gives

$$2\left(\Omega + \frac{V}{r}\right)\frac{\partial V}{\partial z} = -\frac{g}{\rho_0}\frac{\partial \rho_B}{\partial r}(= N_r^2), \tag{2.5}$$

where it has been assumed that the vertical component of (2.2) is described by hydrostatic balance. In other words, (2.5) represents a modified thermal wind relation (Shakespeare 2016), where the centripetal, Coriolis and pressure gradient forces are in balance. In the limit of $V/r \to 0$, (2.5) recovers the well-known geostrophic balance (Vallis 2017). In this study, however, the curvature effects are retained in the relation between the vertical gradient of momentum and the horizontal stratification. A schematic of the base flow in thermal wind balance is shown in figure 1.

2.2. *Local stability equations*

To study the stability properties of the base flow in § 2.1, we superimpose small perturbations to write the net flow field as

$$\boldsymbol{u} = \boldsymbol{u}_B + \boldsymbol{u}', \quad \rho = \rho_B + \rho', \quad p = p_B + p', \tag{2.6a–c}$$

where the prime denotes perturbation quantities. The linearized, viscous governing equations for the perturbation flow field are

$$\nabla \cdot \boldsymbol{u}' = 0, \tag{2.7}$$

$$\frac{\mathrm{d}\boldsymbol{u}'}{\mathrm{d}t} + \nabla \boldsymbol{u}_B \cdot \boldsymbol{u}' + 2\Omega \boldsymbol{e}_z \times \boldsymbol{u}' + \nabla p' = \nu \nabla^2 \boldsymbol{u}' - b' e_z, \tag{2.8}$$

$$\frac{\mathrm{d}b'}{\mathrm{d}t} + \boldsymbol{u}' \cdot \nabla \rho_B \frac{g}{\rho_o} = \kappa \nabla^2 b', \tag{2.9}$$

where $b' = g\rho'/\rho_0$, and the base flow has been assumed to satisfy the inviscid governing equations. In other words, (2.7)–(2.9) represent the governing equations for small, viscous perturbations superimposed on the inviscid base flow described in § 2.1. Here, $\mathrm{d}/\mathrm{d}t = \partial/\partial t + \boldsymbol{u}_B \cdot \nabla$ is the material time derivative in the base flow $\boldsymbol{u}_B$.

In accordance with the local stability approach (Lifschitz & Hameiri 1991), we assume short-wavelength perturbations of the form

$$\boldsymbol{u}' = \exp(\mathrm{i}\phi(\boldsymbol{x}, t)/\delta)[\boldsymbol{a}(\boldsymbol{x}, t) + \delta \boldsymbol{a}_\delta(\boldsymbol{x}, t) + \ldots], \tag{2.10}$$

$$p' = \exp(\mathrm{i}\phi(\boldsymbol{x}, t)/\delta)[\pi(\boldsymbol{x}, t) + \delta \pi_\delta(\boldsymbol{x}, t) + \ldots], \tag{2.11}$$

$$b' = \exp(\mathrm{i}\phi(\boldsymbol{x}, t)/\delta)[b(\boldsymbol{x}, t) + \delta b_\delta(\boldsymbol{x}, t) + \ldots], \tag{2.12}$$

where δ is a small 'short-wavelength' parameter, and $\phi(\boldsymbol{x}, t)$ is a real scalar field that contains the wave-like behaviour in the perturbations. The perturbation wave vector $\boldsymbol{k}'$ is given by $\boldsymbol{k}' = \nabla\phi/\delta = \boldsymbol{k}/\delta$, thus rendering the perturbation to be of short wavelength since δ is a small parameter; $(\boldsymbol{a}, \pi, b)$ are the complex leading-order amplitudes of the velocity, pressure and buoyancy perturbations, respectively. Similarly, $(\boldsymbol{a}_\delta, \pi_\delta, b_\delta)$ are the complex perturbation amplitudes at $O(\delta)$.

Assuming the two diffusivities ν and κ to be of $O(\delta^2)$, and substituting the perturbation forms in (2.10)–(2.12) in the governing equations (2.7)–(2.9), results at $O(\delta^0)$ in the local stability equations

$$\frac{\mathrm{d}\boldsymbol{k}}{\mathrm{d}t} = -\nabla \boldsymbol{u}_B^{\mathrm{T}} \cdot \boldsymbol{k}, \tag{2.13}$$

$$\frac{\mathrm{d}\boldsymbol{a}}{\mathrm{d}t} = -\nabla \boldsymbol{u}_B \cdot \boldsymbol{a} - 2\Omega \boldsymbol{e}_z \times \boldsymbol{a} - b\boldsymbol{e}_z + \frac{\boldsymbol{k}}{|\boldsymbol{k}|^2}[2(\nabla \boldsymbol{u}_B \cdot \boldsymbol{a}) \cdot \boldsymbol{k} + 2(\Omega \boldsymbol{e}_z \times \boldsymbol{a}) \cdot \boldsymbol{k} + bk_z] - c_\nu |\boldsymbol{k}|^2 \boldsymbol{a}, \tag{2.14}$$

$$\frac{\mathrm{d}b}{\mathrm{d}t} = -(\boldsymbol{a} \cdot \nabla \rho_B)\frac{g}{\rho_0} - c_\kappa |\boldsymbol{k}|^2 b. \tag{2.15}$$

In (2.13)–(2.15), $\mathrm{d}/\mathrm{d}t = \partial/\partial t + \boldsymbol{u}_B \cdot \nabla$ is the material time derivative in the base flow $\boldsymbol{u}_B$, k_z the z-component of $\boldsymbol{k}$, and $(c_\nu, c_\kappa) = (\nu, \kappa)/\delta^2$. The assumptions of ν and κ being of $O(\delta^2)$ are motivated by the second-order spatial gradients in the viscous terms, which then contribute at $O(\delta^0)$ in (2.8)–(2.9). Previous studies on local instabilities have incorporated viscous effects in this manner. For example, (2.13)–(2.14) without background rotation and buoyancy were considered by Landman & Saffman (1987), who showed that viscous terms suppress the growth rates associated with elliptic instability in an unstratified, planar elliptical vortex. In addition to elucidating viscous damping of inviscid instabilities, the $O(\delta^2)$ scaling of momentum and mass diffusivities have helped the local approach unearth double-diffusive instabilities in stratified vortices as well (Kirillov & Mutabazi 2017; Singh

& Mathur 2019). Finally, the $O(\delta^2)$ scaling for temperature and salinity diffusivities also leads to the reduction of local stability equations to the classical salt fingering instability equation for a quiescent base flow (Appendix A).

In the absence of diffusive effects ($c_\nu = c_\kappa = 0$), (2.13)–(2.15) coincide with the equations considered by Miyazaki (1993) for a stably stratified elliptical vortex with no in-plane stratification; further, if background rotation is also absent, (2.13)–(2.15) reduce to those considered by Miyazaki & Fukumoto (1992). Finally, if background rotation and buoyancy are both absent, (2.13)–(2.14) coincide with those derived by Lifschitz & Hameiri (1991). The equations governing the evolution of $\boldsymbol{a}$ and b are solved on closed fluid particle trajectories in the base flow for periodic wave vectors, to subsequently obtain corresponding growth rates. We proceed to obtain the conditions under which perturbation wave vectors are periodic upon integrating the wave vector evolution equation (2.13) over a closed trajectory in the base flow given by (2.4). For a wave vector $\boldsymbol{k} = k_r\boldsymbol{e}_r + k_\omega\boldsymbol{e}_\omega + k_z\boldsymbol{e}_z$, (2.13) can be written in component form as

$$\frac{\mathrm{d}k_r}{\mathrm{d}t} = k_\omega\frac{V}{r} - \frac{\partial V}{\partial r}k_\omega, \tag{2.16}$$

$$\frac{\mathrm{d}k_\omega}{\mathrm{d}t} = 0, \tag{2.17}$$

$$\frac{\mathrm{d}k_z}{\mathrm{d}t} = -\frac{\partial V}{\partial z}k_\omega. \tag{2.18}$$

Equation (2.17) indicates that k_ω is a constant along the trajectory, and a non-zero value for the constant would lead to a monotonically changing k_r and k_z. Therefore, for each of k_r, k_ω and k_z to be periodic upon integration over one closed trajectory, k_ω has to necessarily be zero. With $k_\omega = 0$, k_r and k_z become constant along the trajectory. It is noteworthy that $k_\omega = 0$ represents zero azimuthal wavenumber, i.e. axisymmetric perturbations in the normal mode approach, although the perturbation amplitudes are still allowed to evolve along the circular base flow trajectory in the local stability approach. In summary, any wave vector given by $\boldsymbol{k} = k_r\boldsymbol{e}_r + k_z\boldsymbol{e}_z$ represents a periodic wave vector; the amplitude evolution equations (2.14)–(2.15) are solved for such periodic wave vectors. The periodicity of the wave vector enables the use of Floquet theory to obtain growth rates, and ensures uniqueness of the perturbation wave vector at a given spatial location. The latter aspect is potentially relevant for establishing a connection between local and global stability approaches.

For the base flow in (2.4), considering periodic wave vectors, (2.14)–(2.15) can be written in cylindrical polar coordinates as

$$\frac{\mathrm{d}(\boldsymbol{a}|b)}{\mathrm{d}t} = \boldsymbol{A}(\boldsymbol{a}|b), \tag{2.19}$$

where $(\boldsymbol{a}|b) = [a_r, a_\omega, a_z, b]^{\mathrm{T}}$ and $\boldsymbol{A}$ is a 4×4 matrix. Substituting $\boldsymbol{a} = a_r\boldsymbol{e}_r + a_\omega\boldsymbol{e}_\omega + a_z\boldsymbol{e}_z$ and a periodic wave vector $\boldsymbol{k} = k_r\boldsymbol{e}_r + k_z\boldsymbol{e}_z$ in (2.14)–(2.15), we obtain

$$\boldsymbol{A} = \begin{bmatrix} -c_\nu|\boldsymbol{k}|^2 & 2\left(\dfrac{V}{r}+\Omega\right)\left(1-\dfrac{k_r^2}{|\boldsymbol{k}|^2}\right) & 0 & \dfrac{k_rk_z}{|\boldsymbol{k}|^2} \\ -\left(\dfrac{\partial V}{\partial r}+\dfrac{V}{r}+2\Omega\right) & -c_\nu|\boldsymbol{k}|^2 & -\dfrac{\partial V}{\partial z} & 0 \\ 0 & -\dfrac{2k_zk_r}{|\boldsymbol{k}|^2}\left(\dfrac{V}{r}+\Omega\right) & -c_\nu|\boldsymbol{k}|^2 & -\left(1-\dfrac{k_z^2}{|\boldsymbol{k}|^2}\right) \\ N_r^2 & 0 & N_z^2 & -c_\kappa|\boldsymbol{k}|^2 \end{bmatrix}, \tag{2.20}$$

where $\mathrm{d}\boldsymbol{e}_r/\mathrm{d}t = \boldsymbol{e}_\omega V/r$ and $\mathrm{d}\boldsymbol{e}_\omega/\mathrm{d}t = -\boldsymbol{e}_r V/r$ have been used to account for circular fluid particle trajectories with an angular speed V/r. Owing to the constancy of r and V on a streamline, and k_r, k_z, $|\boldsymbol{k}|$ also being invariant along a streamline for periodic wave vectors, the coefficient matrix $\boldsymbol{A}$ in (2.20) is time independent.

3. Results

The eigenvalues (λ) of $\boldsymbol{A}$ (2.20) represent the growth rates, and are governed by

$$(c_\nu|\boldsymbol{k}|^2+\lambda)\left\{(c_\nu|\boldsymbol{k}|^2+\lambda)^2(c_\kappa|\boldsymbol{k}|^2+\lambda)+(c_\nu|\boldsymbol{k}|^2+\lambda)\left[N_z^2\left(1-\frac{k_z^2}{|\boldsymbol{k}|^2}\right)-N_r^2\frac{k_rk_z}{|\boldsymbol{k}|^2}\right]\right.$$
$$+(c_\kappa|\boldsymbol{k}|^2+\lambda)\left[-2\frac{\partial V}{\partial z}\left(\frac{V}{r}+\Omega\right)\frac{k_rk_z}{|\boldsymbol{k}|^2}\right.$$
$$\left.\left.+2\left(\frac{\partial V}{\partial r}+\frac{V}{r}+2\Omega\right)\left(\frac{V}{r}+\Omega\right)\left(1-\frac{k_r^2}{|\boldsymbol{k}|^2}\right)\right]\right\}=0. \tag{3.1}$$

The growth rate σ is given by the maximum real part of λ, which we analyse in detail in the rest of this paper. Instabilities with zero or non-zero imaginary part in the corresponding eigenvalues are henceforth referred to as monotonic or oscillatory, respectively. In the presence of diffusion terms ($c_\nu > 0$, $c_\kappa > 0$), one of the eigenvalues of $\boldsymbol{A}$ is $-c_\nu|\boldsymbol{k}|^2$, while the other three eigenvalues of $\boldsymbol{A}$ can be given by a cubic equation. Dividing by $|\Phi/2|^{3/2}$, (3.1) is non-dimensionalized to give the governing equation for the other three eigenvalues as

$$(\tilde{\lambda}+\tilde{c})^3+\tilde{c}\left(\frac{1-Sc}{Sc}\right)(\tilde{\lambda}+\tilde{c})^2+2\hat{\Phi}(\cos^2\theta+\tan\Theta\tan\Gamma\sin^2\theta$$
$$-\tan\Gamma\sin 2\theta)(\tilde{\lambda}+\tilde{c})+\tilde{c}\left(\frac{1-Sc}{Sc}\right)2\hat{\Phi}\left(\cos^2\theta-\frac{\tan\Gamma}{2}\sin 2\theta\right)=0, \tag{3.2}$$

where

$$\Phi=2\left(\frac{V}{r}+\Omega\right)\left(\frac{\partial V}{\partial r}+\frac{V}{r}+2\Omega\right), \tag{3.3}$$

where $\tilde{\lambda}=\lambda/\sqrt{|\Phi/2|}$, $\hat{\Phi}=\Phi/|\Phi|$ and $Sc=\nu/\kappa=c_\nu/c_\kappa$ is the Schmidt number. As shown in § 3.2, $\hat{\Phi}=-1$ corresponds to centrifugal instability in the inviscid limit. With this choice of non-dimensionalization, the important limit of weak (but finite) viscous effects is easily recovered without the divergence of non-dimensionalized growth rate.

The non-dimensional parameters that appear in (3.2) are

$$\tan\Gamma=\frac{N_r^2}{\Phi},\quad \tan\Theta=\frac{N_z^2}{N_r^2}, \tag{3.4a,b}$$

$$\theta=\cos^{-1}\frac{k_z}{|\boldsymbol{k}|},\quad \tilde{c}=\frac{c_\nu|\boldsymbol{k}|^2}{\sqrt{|\Phi/2|}}, \tag{3.5a,b}$$

where (Γ,Θ) in (3.4a,b) describe the base flow, and $(\theta,\tilde{c})$ in (3.5a,b) describe the perturbation wave vector. Φ, as defined in (3.3), is the Rayleigh discriminant, i.e. twice the product between the total angular velocity and the absolute vertical vorticity in the base flow. Specifically, Γ is a measure of the vertical velocity gradient (recall that

$N_r^2 = 2(\Omega + V/r)\partial V/\partial z$ due to thermal wind balance) with respect to the strength of centrifugal instability in the inviscid, unstratified limit (see § 3.2), and Θ is the inclination of the isopycnals with respect to the z-axis in the base flow. In (3.5*a*,*b*), θ is the inclination of the perturbation wave vector with respect to the z-axis, and $\tilde{c}$ is the inverse of a perturbation Reynolds number, which quantifies the viscous effects in the perturbation with respect to the inertia in the base flow. It is worth noting that the non-dimensional parameters in (3.4*a*,*b*)–(3.5*a*,*b*) are defined such that the inviscid limit can be recovered without any singularities. In addition to the four parameters in (3.4*a*,*b*)–(3.5*a*,*b*), Sc is also a parameter that appears in (3.2), thus influencing the instability characteristics. As shown in § 3.4, for given values of ($\tan\Gamma$, $\tan\Theta$, θ, $\tilde{c}$, Sc), monotonic and oscillatory instabilities cannot occur simultaneously.

3.1. *Comparison with McIntyre (1970)*

McIntyre (1970) considered a base flow similar to the current study, described by a purely azimuthal velocity field $V_M(r, z)\boldsymbol{e}_\omega$ and a potential temperature field $T_M(r, z)$, under the influence of background rotation $\Omega\boldsymbol{e}_z$, gravity $-g\boldsymbol{e}_z$ and in thermal wind balance. Defining $C_M(r, z) = 2\Omega r + V_M(r, z)$, McIntyre (1970) identified the following non-dimensional base flow parameters:

$$\tan\Gamma_M = \frac{C_{M,z}}{C_{M,r}}, \quad \tan\Theta_M = \frac{T_{M,z}}{T_{M,r}}, \tag{3.6a,b}$$

with the Schmidt number being given by $Sc = \nu/\kappa$. In (3.6*a*,*b*), the subscripts z and r denote differentiation with respect to z and r, respectively.

Operating in the regime $N_z^2 = g\alpha T_{M,z} > 0$ (statically stable, with α being the thermal expansion coefficient), $2\Omega C_{M,r} > 0$ (centrifugally stable in locally Cartesian coordinates), McIntyre (1970) considered a locally Cartesian (curvature effects ignored) unbounded normal mode theory (Wentzel–Kramers–Brillouin–Jeffreys, i.e. WKBJ-type approximation where spatial gradients of the base flow are assumed constant). Considering perturbations of the form $\exp[\mathrm{i}k_M(r\sin\theta + z\cos\theta) + \omega_M t]$, with θ being the angle between the wave vector and the z-axis, the author derived the governing equation for the non-dimensional growth rate as

$$(\omega_M + k_M^2)^2(\omega_M + Sc^{-1}k_M^2) + (G + J)\omega_M + (G + Sc^{-1}J)k_M^2 = 0, \tag{3.7}$$

where $\mathrm{Re}(\omega_M)$ is the growth rate, k_M is the magnitude of the wave vector, $G = s(\tan\Theta_M \sin^2\theta - \sin\theta\cos\theta)$, $J = s(\cot\Gamma_M \cos^2\theta - \sin\theta\cos\theta)$ and $s = \mathrm{sgn}(\tan\Gamma_M) = \mathrm{sgn}(\tan\Theta_M)$. The criteria for monotonic and oscillatory instabilities were then shown to be $\tan\Theta_M/\tan\Gamma_M < (1 + Sc)^2/4Sc$ and $\tan\Theta_M/\tan\Gamma_M < (3Sc + 1)^2/8Sc(Sc + 1)$, respectively. These criteria can be recovered as the zero curvature limit of our results in § 3.3.3.

To explore the relation between our local stability framework, and McIntyre's theory, we re-write (3.2) in the limit of zero curvature and non-dimensionalization using the length and time scales of McIntyre (1970). Specifically, defining $L = (\nu^2/|N_r^2|)^{1/4}$ and $T = (|N_r^2|)^{-1/2}$ as the length and time scales, (3.2) can be written as

$$\left(\hat{\lambda} + \frac{\hat{k}^2}{\delta^2}\right)^2\left(\hat{\lambda} + Sc^{-1}\frac{\hat{k}^2}{\delta^2}\right) + s[\tan\Theta_M \sin^2\theta + \cot\Gamma_M \cos^2\theta - 2\sin\theta\cos\theta]\hat{\lambda}$$

$$+ s[\tan\Theta_M \sin^2\theta - \sin\theta\cos\theta + Sc^{-1}(\cot\Gamma_M \cos^2\theta - \sin\theta\cos\theta)]\frac{\hat{k}^2}{\delta^2} = 0, \tag{3.8}$$

where $\hat{\lambda} = \lambda T$, $\hat{k} = \boldsymbol{k}L$ and $\nu = c_\nu \delta^2$ is the kinematic viscosity as defined in § 2.2; $\hat{\Phi} = 1$ has been assumed. We note that $\hat{\Phi} = 1$ is equivalent to $2\Omega C_{M,r} > 0$, i.e. the study of McIntyre (1970) is restricted to the first and third quadrants of the $(\tan \Gamma, \tan \Theta)$ plane. Equation (3.8) is the same as (3.7), with $k_M = \hat{k}/\delta$. Thus, we have shown that, in the limit of zero curvature, the local stability equation for the growth rate concurs with the locally Cartesian unbounded normal mode theory. This connection between local stability and normal mode approaches builds on previous such connections demonstrated for other flows: inviscid, unstratified axisymmetric vortices with an axial flow (Le Duc & Leblanc 1999; Mathur *et al.* 2014), viscous unstratified elliptical vortex (Landman & Saffman 1987) and viscous, in-plane stratified axisymmetric flow with an arbitrary Prandtl number (Kirillov & Mutabazi 2017).

Apart from our study being based on a different approach compared with McIntyre (1970), our results are also wider in scope compared with the results of McIntyre (1970) in three significant aspects: (i) exploration in the centrifugally unstable regime (second and fourth quadrants of $(\tan \Gamma, \tan \Theta)$ plane), (ii) viscous instability characteristics away from the neutral stability boundaries in both the centrifugally stable and unstable regimes and (iii) curvature effects. With respect to point (ii), we note that the length scale L used by McIntyre (1970) for non-dimensionalization makes it difficult to explore the regime of small but finite viscous effects. As discussed in § 3.3, significant growth rates of both monotonic and oscillatory instabilities can occur in the weakly viscous regime, where even the most unstable perturbations can lie. The curvature effects are discussed more in detail in § 4.1.

3.2. *Inviscid limit*

Substituting the inviscid limit of $c_\nu = c_\kappa = 0$ in (3.1), the non-trivial roots are obtained as

$$\lambda^2 = -\frac{1}{2}(N_z^2 + \Phi) + \frac{1}{2}(N_z^2 - \Phi)\cos 2\theta + \left(\frac{N_r^2}{2} + \frac{\partial V}{\partial z}\left(\frac{V}{r} + \Omega\right)\right)\sin 2\theta, \tag{3.9}$$

where $\theta \in [0, \pi]$ is the angle made by the wave vector $\boldsymbol{k}$ with the z-axis, such that $k_z/|\boldsymbol{k}| = \cos\theta$ and $k_r/|\boldsymbol{k}| = \sin\theta$. Maximizing λ^2 with respect to θ, and requiring it to be positive results in the following inviscid instability criterion:

$$N_z^2 \Phi < 2N_r^2 \left(\frac{V}{r} + \Omega\right)\frac{\partial V}{\partial z} (= N_r^4). \tag{3.10}$$

As a result, $\Phi < 0$ (in other words, $\hat{\Phi} = -1$) guarantees instability (recall that $N_z^2 > 0$ is assumed). The maximum growth rate occurs at

$$\theta^* = \begin{cases} \dfrac{\pi}{4} - \frac{1}{2}\tan^{-1}(N_z^2 - \Phi)/2N_r^2, & \text{if } N_r^2 \geq 0 \\ \dfrac{3\pi}{4} - \frac{1}{2}\tan^{-1}(N_z^2 - \Phi)/2N_r^2, & \text{if } N_r^2 < 0, \end{cases} \tag{3.11}$$

where the range of $\tan^{-1}$ is taken to be $[-\pi/2, \pi/2]$. We recall from (2.5) that thermal wind balance requires $N_r^2 = 2(V/r + \Omega)(\partial V/\partial z)$. The ranges of unstable θ are given by

$$[\theta_1, \theta_2], \text{ if } N_r^2, \Phi > 0, \quad [0, \theta_1] \cup [\theta_2 + \pi, \pi], \text{ if } N_r^2 > 0, \Phi < 0, \tag{3.12}$$

$$[\theta_2 + \pi, \theta_1 + \pi], \text{ if } N_r^2 < 0, \Phi > 0, \quad [0, \theta_2] \cup [\theta_1 + \pi, \pi], \text{ if } N_r^2, \Phi < 0, \tag{3.13}$$

where

$$\theta_{1,2} = \tan^{-1}\left\{\frac{N_r^2}{N_z^2}\left[1 \mp \sqrt{1 - \frac{N_z^2\Phi}{N_r^4}}\right]\right\}, \tag{3.14}$$

where we have again taken the range of $\tan^{-1}$ as $[-\pi/2, \pi/2]$.

The results in (3.10) and (3.11), in the limit of no curvature effects, i.e. $V/r = 0$, are in agreement with the previously known two-dimensional inviscid symmetric instability criteria derived based on the normal mode approach (Ooyama 1966; Hoskins 1974). To the best of our knowledge, recovery of the symmetric instability criteria in the local stability framework has not been pointed out before. Furthermore, (3.10)–(3.14) provide corrections due to finite curvature effects, which are difficult to capture in the normal mode approach (Buckingham *et al.* 2021*a*) although they are negligible only in the limit of $|V/r| \ll |\Omega|$. Equation (3.10), which is in agreement with the symmetric instability criterion based on Lagrangian parcel arguments (Solberg 1936; Emanuel 1979) and the recent studies of Buckingham *et al.* (2021*a*,*b*), also establishes the local stability framework as an alternative approach to understand curvature effects. Finally, an insightful interpretation of (3.10) is that the square of the absolute circulation $(2\pi(\Omega r^2 + Vr))$ decreases with radius when moving along iso-density surfaces (Emanuel 1979); this form of the symmetric instability criterion has been previously used to interpret instabilities in pancake vortices (Negretti & Billant 2013; Yim & Billant 2016; Yim, Billant & Ménesguen 2016).

In the limit of no radial stratification, i.e. $N_r = 0$, the instability criterion in (3.10) reduces to $\Phi < 0$, with the maximum growth rate being given by $\lambda^* = \sqrt{-\Phi}$ occurring at $\theta^* = 0$. This no-radial-stratification inviscid limit was highlighted using the local stability approach by Singh & Mathur (2019), and is consistent with the large axial wavenumber limit of Billant & Gallaire (2005). In this unstable regime of $\Phi < 0$, the range of unstable θ reduces from $[0, \pi/2]$ for $N_z = 0$ to $[0, \tan^{-1}\sqrt{-\Phi/N_z^2}]$ for a finite N_z. Finally, in the limit of a homogeneous fluid, i.e. $N_r = N_z = 0$, (3.9) gives the classical inviscid centrifugal instability criterion (Kloosterziel & Van Heijst 1991). This limit of centrifugal instability in unstratified vortices with background rotation has been considered in previous local stability studies too (Sipp & Jacquin 2000; Nagarathinam, Sameen & Mathur 2015).

In terms of the non-dimensional base flow parameters in (3.4*a*,*b*), the inviscid instability criterion in (3.10) can be written as

$$\frac{\tan\Theta}{\tan\Gamma} < 1, \tag{3.15}$$

with the most unstable θ given by

$$\theta^* = \begin{cases} \dfrac{\pi}{4} - \frac{1}{2}\tan^{-1}\{\tan\Theta/2 - 1/(2\tan\Gamma)\}, & \text{if } N_r^2 \geq 0 \\ \dfrac{3\pi}{4} - \frac{1}{2}\tan^{-1}\{\tan\Theta/2 - 1/(2\tan\Gamma)\}, & \text{if } N_r^2 < 0. \end{cases} \tag{3.16}$$

It is worth highlighting that

$$\frac{\tan\Theta}{\tan\Gamma} = \frac{\Phi N_z^2}{N_r^4} = \frac{N_z^2}{(\partial V/\partial z)^2}\frac{(\partial V/\partial r + V/r + 2\Omega)}{2(\Omega + V/r)} \tag{3.17}$$

represents a modified gradient Richardson number. The inviscid instability regimes on the $(\tan\Gamma, \tan\Theta)$ plane are shown in figure 2. In the first and third quadrants, $\tan\Theta = \tan\Gamma$

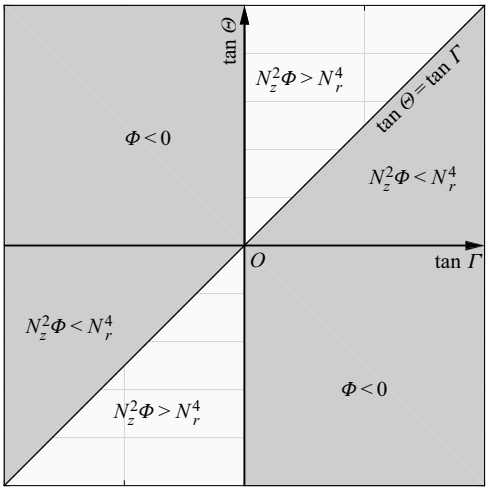

Figure 2. Inviscidly stable (white background) and unstable (grey background) regions on the (tan Γ, tan Θ) plane. The origin O is at (tan Γ, tan Θ) = (0, 0).

separates the stable and unstable regions, whereas the entire second and fourth quadrants ($\Phi < 0 = \hat{\Phi} = -1$ in these quadrants) are unstable. It is worth recalling that all inviscid instabilities are monotonic in nature (zero imaginary part for the growth rate).

3.3. *Viscous regime*

In the limit of $Sc = 1$, the solutions of (3.2) are $\tilde{\lambda} = -\tilde{c}, \pm[-\hat{\Phi}\{(1 + \tan\Theta \tan\Gamma) + (1 - \tan\Theta \tan\Gamma)\cos 2\theta - 2\tan\Gamma \sin 2\theta\}]^{1/2} - \tilde{c}$. The corresponding dimensional values of λ are $\lambda = -c_\nu|\boldsymbol{k}|^2$, $\lambda = \lambda_i - c_\nu|\boldsymbol{k}|^2$, where λ_i are the inviscid eigenvalues given by (3.9). In other words, for $Sc = 1$, all the eigenvalues from the inviscid limit get reduced by $c_\nu|\boldsymbol{k}|^2$, thus resulting in the inviscid growth rates being reduced by viscous effects, and the occurrence of two stable eigenvalues ($= -c_\nu|\boldsymbol{k}|^2$). As a consequence, the eigenvalues for $Sc = 1$ and $|\boldsymbol{k}| = 0$ coincide with the inviscid eigenvalues, thus establishing an equivalence between inviscid instabilities and instabilities at $Sc = 1$.

For $Sc \neq 1$, three non-trivial eigenvalues governed by (3.2) occur. While two of them could possibly be a continuous extension of the two non-trivial eigenvalues from the inviscid limit, the counterpart of the third eigenvalue was trivial and stable in the inviscid limit. For $Sc \neq 1$, we proceed to plot the non-dimensionalized growth rate ($\tilde{\sigma} = \sigma/\sqrt{|\Phi/2|}$) as a function of the perturbation parameters (3.5*a*,*b*) for given base flow parameters (3.4*a*,*b*). As highlighted earlier in this section, our choice of non-dimensionalization allows us to easily explore the important regime of weak but finite viscous effects.

Figure 3 shows the growth rate (in log scale) plotted as a function of θ and $\tilde{c}$ for tan $\Gamma = 1$, and three different values of tan Θ (1.2, 1 and 0.4), which progressively takes the system from stable to neutrally stable to unstable in the inviscid limit (see first quadrant of figure 2). We recall from (3.15) that tan Θ/ tan $\Gamma < 1$ is the inviscid instability criterion, which also holds for $Sc = 1$. It is also worth noting that for $Sc = 1$, the instability is always monotonic in nature. In figure 3, panels (*a*,*b*,*c*) and (*d*,*e*,*f*) correspond to $Sc = 0.1$ and 5, respectively.

For tan $\Theta = 1.2$ (figure 3*a*), i.e. the inviscidly stable regime, we observe unstable growth rates at $Sc = 0.1$ though no instabilities occur for $Sc = 1$. The monotonic and oscillatory

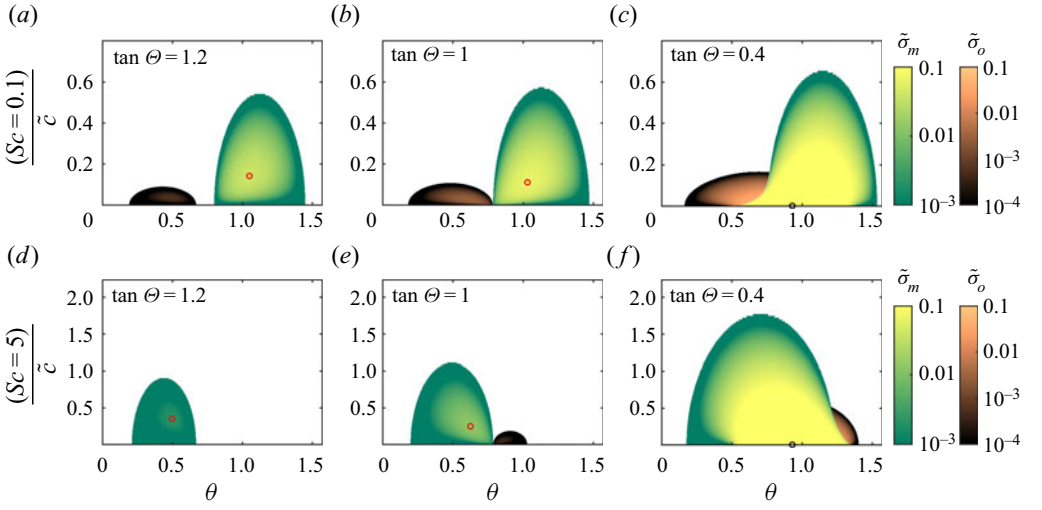

Figure 3. Growth rate ($\tilde{\sigma}$, on a log scale) as a function of θ and $\tilde{c}$ for $Sc = 0.1$ (*a–c*) and $Sc = 5$ (*d–f*), with $\tan\Theta = 1.2$, 1 and 0.4 in (*a*,*d*), (*b*,*e*) and (*c*,*f*), respectively. All the plots correspond to $\tan\Gamma = 1$, thus belonging to the first quadrant of figure 2. The green and brown regions correspond to zero (monotonic instability) and non-zero (oscillatory instability) imaginary part for the growth rate. In each plot, the unfilled circle corresponds to the location of maximum growth rate on the entire (θ, $\tilde{c}$) plane, with the red colour indicating a location away from $\tilde{c} = 0$ axis. No instabilities occur for $\theta > \pi/2$ in all the plots in this figure. The values of $\tan\Theta/\tan\Gamma$ for (*a*,*b*,*d*,*e*) correspond to the inviscidly stable regime, and hence the growth rate is zero on the $\tilde{c} = 0$ axis.

(non-zero imaginary part for the growth rate) instability regions are shown in green and brown, respectively. The monotonic instability dominates the oscillatory instability on the $(\theta, \tilde{c})$ plane, with the overall maximum growth rate occurring at $(\theta^*, \tilde{c}^*) = (1.05\ \text{rad}, 0.14)$ within the monotonic instability region. The monotonic instability is completely suppressed at a threshold value of $\tilde{c}^t = 0.54$. For the oscillatory instability, the maximum growth rate occurs at $(\theta^*, \tilde{c}^*) = (0.49\ \text{rad}, 0.035)$, and it is completely suppressed beyond $\tilde{c} = 0.09$. In terms of the range of θ, monotonic and oscillatory instabilities occur within [0.8,1.45] rad and [0.19,0.67] rad, respectively. The width of these unstable θ ranges are used later (§ 3.3.2) to characterize the instability region on the $(\theta, \tilde{c})$ plane.

For $\tan\Theta = 1$ (figure 3*b*), i.e. on the inviscid neutral stability boundary, monotonic and oscillatory instabilities are again observed at $Sc = 0.1$, with an overall increase in the growth rates compared with $\tan\Theta = 1.2$. The monotonic and oscillatory instability regions are also slightly larger for $\tan\Theta = 1$ than for $\tan\Theta = 1.2$. For $\tan\Theta = 0.4$ and $Sc = 0.1$ (figure 3*c*), i.e. the inviscidly unstable regime, the regions of instability and the associated growth rates are noticeably larger. Furthermore, the maximum growth rate on the entire $(\theta, \tilde{c})$ plane now occurs at $(\theta^*, \tilde{c}^*) = (0.93\ \text{rad}, 0)$, still within the monotonic instability region. For reference, the monotonic instability for $(\tan\Gamma, \tan\Theta) = (1, 0.4)$ at $Sc = 1$ is also strongest at the same $(\theta^*, \tilde{c}^*)$ location (see (3.16)).

Figure 3(*d–f*) corresponds to the same parameters as panels (*a*,*b*,*c*), except for Sc, which is now set at 5. In the inviscidly stable regime of $\tan\Theta = 1.2$ (figure 3*d*), monotonic instability is observed while oscillatory instability is absent. The overall growth rates are smaller in magnitude than for $Sc = 0.1$, and the maximum growth rate occurs at $(\theta^*, \tilde{c}^*) = (0.5\ \text{rad}, 0.35)$. With an increase in $\tan\Theta$ to unity (figure 3*e*), the growth rate magnitudes increase, and oscillatory instability appears. In contrast to $Sc = 0.1$,

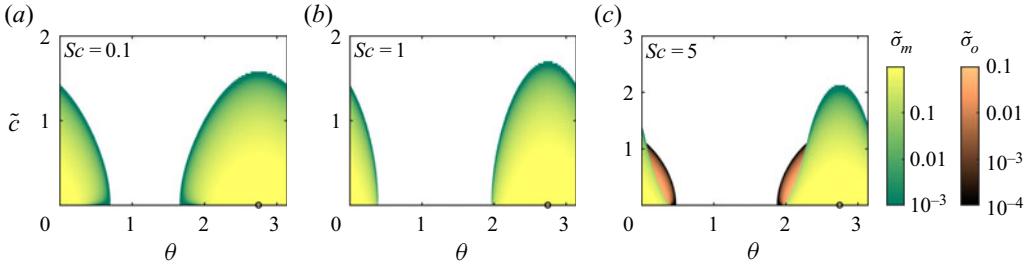

Figure 4. Growth rate ($\tilde{\sigma}$, on a log scale) as a function of θ and $\tilde{c}$ for (*a*) $Sc = 0.01$, (*b*) $Sc = 1$, (*c*) $Sc = 5$, with $(\tan\Gamma, \tan\Theta) = (1, -1)$, and thus belonging to the fourth quadrant in figure 2. The green and brown regions correspond to zero (monotonic instability) and non-zero (oscillatory instability) imaginary part for the growth rate. In each plot, the unfilled circle corresponds to the location of maximum growth rate on the entire $(\theta, \tilde{c})$ plane. In (*c*), the growth rate corresponding to oscillatory instability vanishes on the $\tilde{c} = 0$ axis.

oscillatory instability occurs at larger θ than that for the monotonic instability at $Sc = 5$. Finally, in the inviscidly unstable regime of $\tan\Theta = 0.4$ (figure 3*f*), oscillatory instability again appears alongside the monotonic instability, the region of instability on the $(\theta, \tilde{c})$ plane is substantially larger than for smaller $\tan\Theta$, and the maximum growth rate occurs at the same $(\theta^*, \tilde{c}^*) = (0.93 \text{ rad}, 0)$ as that for the monotonic instability at $Sc = 1$.

In summary of figure 3, for $Sc \neq 1$, monotonic instability appears in the inviscidly stable regime too, while a new oscillatory instability appears in inviscidly stable as well as unstable regimes. The maximum growth rate on the $(\theta, \tilde{c})$ plane, however, always lies in the monotonic instability region, irrespective of Sc, $\tan\Gamma$ and $\tan\Theta$. We show later in §§ 3.3.3 and 3.4 that the monotonic instability observed for $Sc \neq 1$ is a continuous extension of the monotonic symmetric instability that occurs at both $Sc = 1$ and the inviscid limit. We proceed to investigate (in figure 4) the instabilities for $Sc \neq 1$ in the fourth quadrant of figure 2, the entirety of which is inviscidly unstable due to $\Phi < 0$.

Figure 4(*a*,*b*) shows that only monotonic instability occurs at $Sc = 0.1$ and $Sc = 1$ for $(\tan\Gamma, \tan\Theta) = (1, -1)$. The range of unstable θ is noticeably larger for $Sc = 0.1$ compared with $Sc = 1$. At $Sc = 5$ (figure 4*c*), oscillatory instability appears along with the monotonic instability. Finally, we note that the most unstable $(\theta, \tilde{c})$ is $(2.75 \text{ rad}, 0)$, which lies within the monotonic instability region, for all three Sc in figure 4. Furthermore, we find that the largest growth rate is always associated with the monotonic instability for every unstable $(\tan\Gamma, \tan\Theta, Sc)$. Towards obtaining neutral stability boundaries in terms of the base flow parameters and Sc, we proceed to plot the most unstable growth rate in the monotonic and oscillatory instability regions of plots such as in figures 3 and 4, on the $(\tan\Gamma, \tan\Theta)$ plane.

3.3.1. *Dominant instability characteristics*

The maximum growth rate on the $(\theta, \tilde{c})$ plane, and the corresponding location at which it occurs, are plotted as a function of $\tan\Gamma$ and $\tan\theta$ for $Sc = 0.1$ and 5 in the panels (*a*,*b*,*c*) and (*g*,*h*,*i*) of figure 5, respectively. We recall that the maximum growth rate always corresponds to the monotonic instability. For reference, the equivalent plots for $Sc = 1$ are shown in panels (*d*,*e*,*f*), with the black lines in (*a*,*b*,*d*,*g*,*h*,*i*) representing the boundary separating stable and unstable regions for $Sc = 1$. The panels (*a*,*d*,*g*), (*b*,*e*,*h*) and (*c*,*f*,*i*) show the distributions of maximum growth rate $\tilde{\sigma}^{max}$ (on a log scale), and the most unstable $(\theta, \tilde{c}) = (\theta^*, \tilde{c}^*)$, respectively.

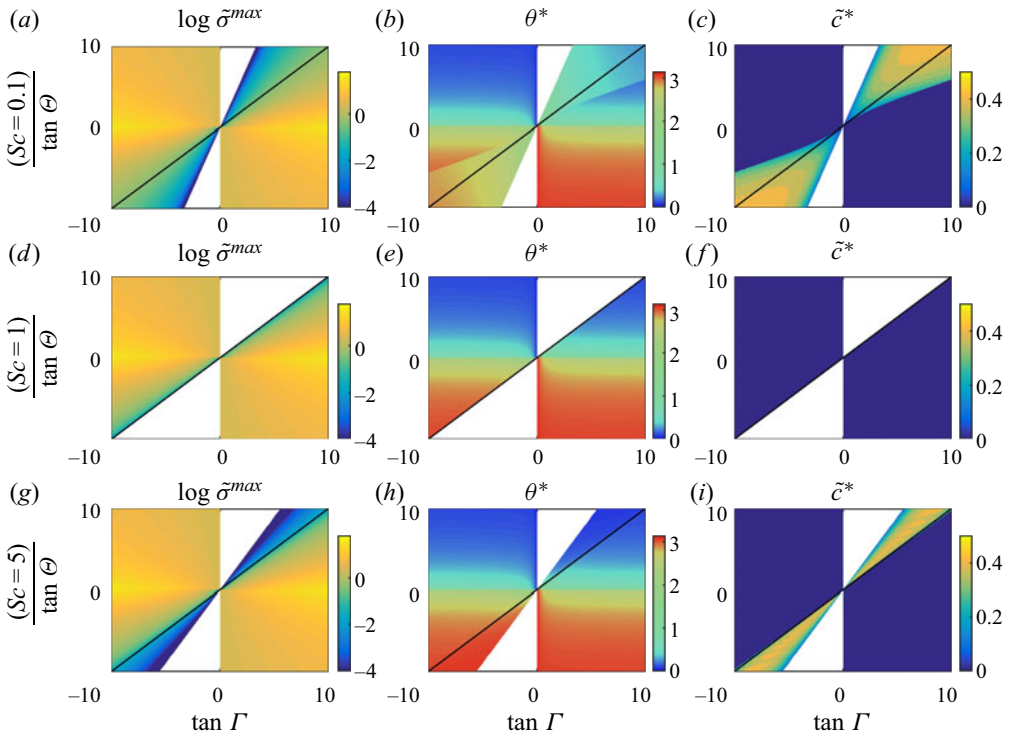

Figure 5. Maximum growth rate ($\log\tilde{\sigma}^{max}$) on the $(\theta, \tilde{c})$ plane, plotted as a function of $\tan\Gamma$ and $\tan\Theta$ for (*a*) $Sc = 0.1$, (*d*) $Sc = 1$ and (*g*) $Sc = 5$. Corresponding locations on the $(\theta, \tilde{c})$ plane where the maximum growth rate occurs are plotted as θ^* (*b*,*e*,*h*) and $\tilde{c}^*$ (*c*,*f*,*i*). The black line in all the plots represents the neutral stability ($\tilde{\sigma}^{max} = 0$) boundary for $Sc = 1$.

For $Sc = 0.1$, monotonic instability is observed in the inviscidly stable region of the first quadrant of the $(\tan\Gamma, \tan\Theta)$ plane, with the neutral stability boundary being steeper than that for $Sc = 1$ (figure 5*a*). In contrast to $Sc = 1$, some part of the monotonic instability region for $Sc = 0.1$ has the maximum growth rate occurring at finite viscous effects, i.e. $\tilde{c}^* > 0$ (figure 5*c*). Interestingly, $\tilde{c}^* > 0$ occurs for the whole of the unstable region that was inviscidly stable, and some part of the inviscidly unstable region as well. The $\tilde{c}^* = 0$ boundary is coincident with a distinct θ^* contour (figure 5*b*), on which the value of θ^* is equal to the inviscid value. The value of θ^* seems to abruptly increase as we enter the $\tilde{c}^* > 0$ region. In the third quadrant of the $(\tan\Gamma, \tan\Theta)$ plane, we observe similar characteristics as in the first quadrant, but with the θ^* variations occurring in the neighbourhood of $\theta^* = \pi$ instead of $\theta^* = 0$. Finally, the characteristics of dominant instability in the second and fourth quadrants of the $(\tan\Gamma, \tan\Theta)$ plane for $Sc = 0.1$ are similar to those for $Sc = 1$.

For $Sc = 5$, some part of the inviscidly stable regions in the first and third quadrants of the $(\tan\Gamma, \tan\Theta)$ plane becomes unstable (figure 5*g*), as observed for $Sc = 0.1$. In contrast to $Sc = 0.1$, however, $\tilde{c}^* > 0$ seems to occur predominantly in the inviscidly stable region for $Sc = 5$. Also, in the first quadrant of the $(\tan\theta, \tan\Gamma)$ plane for $Sc = 5$, θ^* decreases as we move into the $\tilde{c}^* > 0$ region. As observed for $Sc = 0.1$, the dominant instability characteristics in the second and fourth quadrants seem similar to $Sc = 1$ for $Sc = 5$. In summary of figure 5, some parts of inviscidly stable regions become monotonically unstable for $Sc \neq 1$, with the extent of instability depending on the value of Sc. $Sc \neq 1$

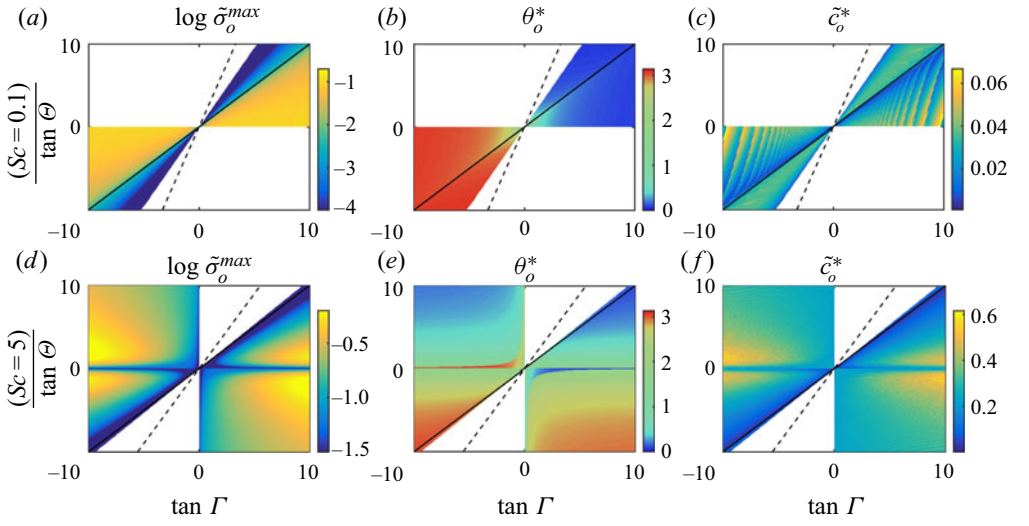

Figure 6. Maximum growth rate ($\log \tilde{\sigma}_o^{max}$) in the oscillatory instability region on the $(\theta, \tilde{c})$ plane, plotted as a function of $\tan\Gamma$ and $\tan\Theta$ for (*a*) $Sc = 0.1$ and (*d*) $Sc = 5$. Corresponding locations on the $(\theta, \tilde{c})$ plane where the maximum oscillatory instability growth rate occurs are plotted as θ_o^* (*b*,*e*) and $\tilde{c}_o^*$ (*c*,*f*). The solid black line in all the plots represents the $\tilde{\sigma}^{max} = 0$ boundary for $Sc = 1$. The black dashed line in all the plots indicates the neutral stability boundary ($\tilde{\sigma}^{max} = 0$, see figure 6) for the respective Sc.

also introduces the occurrence of the maximum growth rate at finite viscous effects, i.e. $\tilde{c}^* > 0$, with such regions showing θ^* distributions that are different from the inviscid limit, i.e. $Sc = 1$.

Figure 6 shows the dominant instability characteristics from within the oscillatory instability regions (brown regions in figures 3 and 4), plotted on the $(\tan\Gamma, \tan\Theta)$ plane for $Sc = 0.1$ (*a–c*) and 5 (*d–f*). We recall that oscillatory instability (non-zero imaginary part for the growth rate) does not occur for $Sc = 1$, and monotonic instability dominates oscillatory instability for each $(\tan\Gamma, \tan\Theta, Sc)$. Figure 6(*a*) shows that the entire inviscidly unstable region in the first quadrant is susceptible to oscillatory instability for $Sc = 0.1$, with the corresponding θ_o^* being around $\pi/2$ close to the origin, and approaching zero for large $(\tan\Gamma, \tan\Theta)$ (figure 6*b*). Figure 6(*c*) shows that oscillatory instability occurs at finite viscous effects ($\tilde{c}_o^* > 0$), with rapid variations observed within the inviscidly unstable region. Some part of the inviscidly stable region is also seen to be susceptible to oscillatory instability, with a growth rate that is much smaller than that for monotonic instability. The extent of oscillatory instability is also smaller than that of monotonic instability, as indicated by the neutral stability boundary (dashed line) in figure 6(*a*). The oscillatory instability features in the third quadrant are similar to those in the first quadrant, with the θ_0^* variations occurring around π rather than 0. Finally, the inviscidly unstable second and fourth quadrants are not affected by oscillatory instability for $Sc = 0.1$.

For $Sc = 5$, the inviscidly unstable region in the first quadrant is again entirely susceptible to the oscillatory instability (figure 6*d*), with $\tilde{\sigma}_o^{max}$, θ_o^* and $\tilde{c}_o^*$ all being relatively large close to the $\tan\Theta = 0$ axis. In addition, there is also a small portion of the inviscidly stable region where oscillatory instability is observed, with the corresponding θ_o^* and $\tilde{c}_o^*$ being close to zero. Finally, in contrast to $Sc = 0.1$, the inviscidly unstable second and fourth quadrants are entirely susceptible to the oscillatory instability for $Sc = 5$. The abrupt changes in θ_o^* close to the $\tan\Theta = 0$ axis in the second and fourth

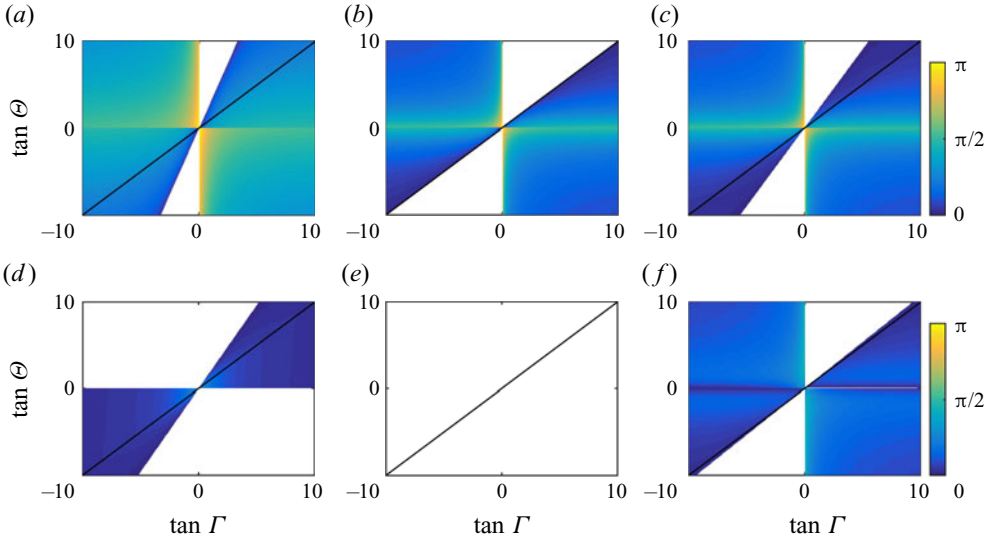

Figure 7. Width of the unstable θ range in the monotonic instability (*a–c*) and oscillatory instability (*d–f*) regions on the $(\theta, \tilde{c})$ plane, plotted as a function of $\tan\Gamma$ and $\tan\Theta$ for (*a,d*) $Sc = 0.1$, (*b,e*) $Sc = 1$ and (*c,f*) $Sc = 5$. The solid black line in all the plots represents the neutral stability boundary ($\tilde{\sigma}^{max} = 0$) for $Sc = 1$.

quadrants of figure 6(*e*) are attributed to the switch of the location of maximum oscillatory instability growth rate from one unstable region to another on the $(\theta, \tilde{c})$ plane (see brown regions in figure 4(*c*) for an example of two disconnected oscillatory instability regions on the $(\theta, \tilde{c})$ plane). For each $(\tan\Gamma, \tan\Theta)$, we proceed to identify the range of unstable θ on the $(\theta, \tilde{c})$ plane for each of the monotonic and oscillatory instabilities. The width of such an unstable range, indicative of the range of perturbation wave vectors that are unstable, is then plotted as a function of $\tan\Gamma$ and $\tan\Theta$ for various Sc, as discussed in § 3.3.2.

3.3.2. *Range of unstable perturbations*

Figure 7 shows the width of unstable θ range on the $(\tan\Gamma, \tan\Theta)$ plane for the monotonic (*a–c*) and oscillatory (*d–f*) instabilities. The panels (*a,d*), (*b,e*) and (*c,f*) correspond to $Sc = 0.1$, 1 and 5, respectively. For $Sc = 1$ (figure 7*b*), monotonic instability occurs in a small range around θ^* (previously shown in figure 5*e*) in the region close to the neutral stability boundary (black line) in the first and third quadrants. The unstable θ width increases as we move away from the neutral stability boundary towards the $\tan\Theta = 0$ axis. In the second and fourth quadrants, a significant range of θ is monotonically unstable near the $\tan\Theta = 0$ and $\tan\Gamma = 0$ axes. In regard to oscillatory instability, as expected, the entire plane of $(\tan\Gamma, \tan\Theta)$ is stable for $Sc = 1$ (figure 7*e*).

In comparison with $Sc = 1$, the width of unstable θ range for monotonic instability is noticeably larger throughout the $(\tan\Gamma, \tan\Theta)$ plane for $Sc = 0.1$ (figure 7*a*). A similar conclusion holds for $Sc = 5$ too (figure 7*c*), with the extent of increase in the width of the unstable θ range being relatively smaller compared with $Sc = 0.1$. For oscillatory instability, the width of unstable θ is, in general, smaller than that for monotonic instability for both $Sc = 0.1$ (figure 7*d*) and 5 (figure 7*f*). For $Sc = 0.1$, the width of the unstable θ range decreases as we move away from the origin (figure 7*d*). For $Sc = 5$, oscillatory instability appears in all the four quadrants of the $(\tan\Gamma, \tan\Theta)$ plane (figure 7*f*), with

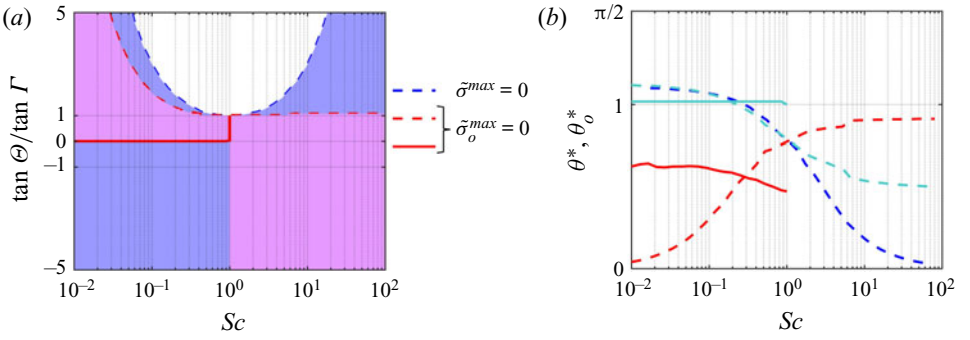

Figure 8. (*a*) Neutral stability boundaries on the (Sc, ($\tan\Theta/\tan\Gamma$)) plane for the overall instability (blue dashed line) and the oscillatory instability (red dashed and solid lines). The blue background indicates region with monotonic instability only, and magenta background indicates regions with monotonic and oscillatory instabilities. (*b*) The wave vector orientation θ^* at which the maximum growth rate occurs on the neutral stability boundaries shown in (*a*). The cyan dashed and the cyan solid lines indicate the θ^* corresponding to monotonic instability along the neutral stability boundaries (red dashed and red solid lines, respectively) for the oscillatory instability.

relatively large width for the unstable θ range occurring in a region slightly shifted away from the $\tan\Theta = 0$ axis. The regions close to $\tan\Gamma = 0$ in the second and fourth quadrants correspond to relatively large width for the unstable θ range of the oscillatory instability, which is similar to what we observed for the monotonic instability in figure 7(*c*).

The neutral stability boundaries in figure 5 ($\tilde{\sigma}^{max} = 0$) and the $\tilde{\sigma}_o^{max} = 0$ boundaries for the oscillatory instability in figure 6 are all observed to be straight lines passing through the origin on the ($\tan\Gamma$, $\tan\Theta$) plane, indicating their dependence only on the ratio $\tan\Theta/\tan\Gamma$. As highlighted in § 3.3, $\tan\Theta/\tan\Gamma$ represents a modified gradient Richardson number. We proceed to investigate the variation (with Sc) of the critical value of $\tan\Theta/\tan\Gamma$ that separates stable and unstable regions.

3.3.3. *Neutral stability boundaries*

Figure 8(*a*) shows the regions of monotonic and oscillatory instabilities on the plane of Sc on the x-axis and $\tan\Theta/\tan\Gamma$ on the y-axis, with the corresponding neutral stability boundaries shown in blue and red, respectively. The neutral stability boundary for the monotonic instability (blue dashed line) also represents the overall neutral stability boundary, thus rendering the region above the blue dashed line stable. The threshold $\tan\Theta/\tan\Gamma$ above which the flow is stable increases as Sc goes away from unity. At $Sc = 0.1$ or 10, the threshold $\tan\Theta/\tan\Gamma$ is around 3.1 times larger than the value at $Sc = 1$. The neutral stability boundary for the oscillatory instability (red dashed line) lies below the overall neutral stability boundary at all $Sc \neq 1$. In contrast to $Sc < 1$. the red dashed line for $Sc > 1$ always remains close to (but above) $\tan\Theta/\tan\Gamma = 1$, reaching a value of 9/8 (see Appendix D) as $Sc \to \infty$. The red solid line captures the lower threshold of $\tan\Theta/\tan\Gamma$ below which oscillatory instability does not occur. For all $Sc < 1$, the red solid boundary occurs below the red dashed boundary, and there exists no red solid boundary for $Sc > 1$, indicating that oscillatory instability occurs for all $Sc \neq 1$. For $Sc < 1$, oscillatory instability occurs between $\tan\Theta/\tan\Gamma = 0$ and the red dashed line, whereas the entire region below the red dashed line is susceptible to oscillatory instability for $Sc > 1$. In other words, a finite ($Sc < 1$) or an infinite ($Sc > 1$) range of $\tan\Theta/\tan\Gamma$ becomes susceptible to oscillatory instability as soon as Sc becomes different from unity.

In the centrifugally unstable regime in the limit of no radial stratification ($\Phi < 0, N_r^2 = 0$), oscillatory instability was previously reported only for $Sc > 1$ (Singh & Mathur 2019), which is consistent with the $\tan\Theta/\tan\Gamma \to -\infty$ limit in figure 8(*a*).

In figure 8(*b*), the blue line shows the variation of θ^*, the location of maximum growth rate, along the overall neutral stability boundary, which is the same as that for the monotonic instability. For $Sc \ll 1$, it is around 1.1 rad, and it decreases towards the inviscid value (3.11) of $\pi/4$ at $Sc = 1$, before decreasing further towards 0.03 rad for $Sc \gg 1$. In contrast, along the neutral stability boundary (red dashed line in figure 8*a*) for the oscillatory instability, θ_o^* increases from around 0.1 rad for $Sc \ll 1$ towards 0.9 rad for $Sc \gg 1$. On the lower neutral stability boundary (red solid line in figure 8a) for the oscillatory instability, θ_o^* is around 0.68 rad for $Sc < 1$. The variation of θ^* corresponding to monotonic instability (cyan dashed and cyan solid lines in figure 8*b*) along the neutral stability boundaries for the oscillatory instability (red dashed and red solid lines in figure 8*a*) indicate that the monotonic and oscillatory instabilities are separated in θ when they occur simultaneously. While not shown in figure 8, the separation in θ between monotonic and oscillatory instabilities has been verified in all the regions where they occur simultaneously. Finally, with respect to $\tilde{c}^*$ and $\tilde{c}_o^*$, they are found to be zero along the neutral stability boundaries for the monotonic (blue dashed line in figure 8*a*) and oscillatory (red dashed line in figure 8*a*) instabilities, respectively. Along the lower neutral stability boundary for the oscillatory instability (red solid line in figure 8*a*), however, $\tilde{c}_o^*$ is finite and varies significantly.

As shown in Appendix D, it is possible to derive closed form expressions for the neutral stability boundaries on the (Sc, ($\tan\Theta/\tan\Gamma$)) plane. The resulting unstable regions are

$$\frac{\tan\Theta}{\tan\Gamma} < \frac{(1+Sc)^2}{4Sc} \tag{3.18}$$

for the monotonic instability, and

$$\left.\begin{aligned} 0 < \frac{\tan\Theta}{\tan\Gamma} < \frac{(3Sc+1)^2}{8Sc(Sc+1)}, \quad \text{if } Sc < 1 \\ \frac{\tan\Theta}{\tan\Gamma} < \frac{(3Sc+1)^2}{8Sc(Sc+1)}, \quad \text{if } Sc > 1 \end{aligned}\right\} \tag{3.19}$$

for the oscillatory instability. In the centrifugally stable regime ($\tan\Theta/\tan\Gamma > 0$) with zero curvature effects, (3.18)–(3.19) coincide with the neutral stability boundaries of McIntyre (1970).

3.4. *Reduction of parameters*

We have thus far presented our results in terms of five different non-dimensional parameters: two of them describing the base flow (3.4*a*,*b*), two more describing the perturbations (3.5*a*,*b*) and Sc. It is, however, possible to choose an alternate non-dimensionalization of (3.1) to further reduce the number of governing non-dimensional parameters, albeit at the cost of not separating the base flow and perturbation characteristics. Specifically, (3.2) can be re-written as

$$\lambda^{*3} + \left(\frac{1-Sc}{Sc}\right)\lambda^{*2} + [\alpha_1 + \alpha_2 - \beta_1 - \beta_2]\lambda^* + \left(\frac{1-Sc}{Sc}\right)[\alpha_1 - \beta_1] = 0, \tag{3.20}$$

where $\lambda^* = (\lambda + c_\nu|\boldsymbol{k}|^2)/(c_\nu|\boldsymbol{k}|^2)$, and

$$\left.\begin{aligned} \alpha_1 &= \frac{\Phi\cos^2\theta}{(c_\nu|\boldsymbol{k}|^2)^2}, \quad \alpha_2 = \frac{N_z^2\sin^2\theta}{(c_\nu|\boldsymbol{k}|^2)^2}, \\ \beta_1 &= \frac{\partial V}{\partial z}\frac{(\Omega + V/r)\sin 2\theta}{(c_\nu|\boldsymbol{k}|^2)^2}, \quad \beta_2 = \frac{N_r^2\sin 2\theta}{2(c_\nu|\boldsymbol{k}|^2)^2}. \end{aligned}\right\} \tag{3.21}$$

In terms of λ^*, instability occurs if $\mathrm{Re}(\lambda^*) > 1$. We also define a non-dimensional growth rate $\bar{\sigma} = \sigma/(c_\nu|\boldsymbol{k}|^2) = \max(\mathrm{Re}(\lambda^*) - 1)$, where σ is the maximum real part of the eigenvalues λ. Unlike the non-dimensionalization used in (3.2), the inviscid limit of $c_\nu = 0$ represents a singularity in (3.20), and hence the weakly viscous limit of $\nu \to 0$ is not easily recovered. Additionally, the thermal wind relation in (2.5) requires $\beta_1 = \beta_2 = \beta$.

Equation (3.20) shows that instability characteristics are dependent only on three different parameters, namely $\alpha_1 - \beta$, $\alpha_2 - \beta$ and Sc. As shown in Appendix B, the neutral stability boundaries for (3.20) are

$$\frac{\alpha_1 - \beta}{Sc} + \alpha_2 - \beta + \frac{1}{Sc} = 0, \quad \text{if } s(\alpha_1 - \beta) < s\frac{1+Sc}{1-Sc}, \tag{3.22}$$

$$2(\alpha_1 - \beta) + (\alpha_2 - \beta)\left(1 + \frac{1}{Sc}\right) + 2\left(1 + \frac{2}{Sc} + \frac{1}{Sc^2}\right) = 0, \quad \text{if } s(\alpha_1 - \beta) > s\frac{1+Sc}{1-Sc}, \tag{3.23}$$

where $s = \mathrm{sgn}(1 - Sc)$. In the limit of $Sc = 1$, the neutral stability boundaries are governed by (3.22) only.

In the unstable neighbourhood ($(\alpha_1 - \beta)/Sc + \alpha_2 - \beta + 1/Sc \lesssim 0$) of the neutral stability boundary in (3.22), the unstable eigenvalue is real, and represents a continuous extension of the inviscid symmetric instability that occurs for $\alpha_1 + \alpha_2 - 2\beta + 1 < 0$. The other two eigenvalues (stable) are either (i) real, if $s(\alpha_1 - \beta) > s/(4Sc(Sc-1))$ or (ii) complex conjugates, if $s(\alpha_1 - \beta) < s/(4Sc(Sc-1))$. In the unstable neighbourhood ($2(\alpha_1 - \beta) + (\alpha_2 - \beta)(1 + 1/Sc) + 2(1 + 2/Sc + 1/Sc^2) \lesssim 0$) of the neutral stability boundary in (3.23), the unstable eigenvalues are complex conjugates, and do not represent a continuous extension of the inviscid or $Sc = 1$ instability; the corresponding instability is an oscillatory instability, based on the non-zero imaginary parts for the unstable eigenvalues. The third eigenvalue is real and stable. Finally, as shown in Appendix C, monotonic and oscillatory instabilities cannot simultaneously occur for given values of $\alpha_1 - \beta$, $\alpha_2 - \beta$ and Sc. As a consequence, even for given values of ($\tan\Gamma$, $\tan\Theta$, θ, $\tilde{c}$, Sc), since α_1, α_2 and β are uniquely specified ($N_z^2 > 0$ assumed), monotonic and oscillatory instabilities cannot occur simultaneously.

Figure 9 shows the neutral stability boundaries on the $((\alpha_1 - \beta), (\alpha_2 - \beta))$ plane for $Sc = 0.1$ (figure 9*a*) and $Sc = 5$ (figure 9*b*). For reference, the neutral stability boundary for $Sc = 1$ (or inviscid instability) is shown in black in figure 9(*a*,*b*). For a given Sc, the neutral stability boundary switches from the monotonic instability (magenta boundary) to the oscillatory instability (red boundary) at $\alpha_1 - \beta = (1 + Sc)/(1 - Sc)$. The normalized growth rate associated with the monotonic instability ($\bar{\sigma}_m$, calculated numerically from (3.20)) increases somewhat rapidly as we move way from its corresponding neutral stability boundary. In contrast, the normalized growth rate associated with the oscillatory instability ($\bar{\sigma}_o$, calculated numerically from (3.20)) remains relatively small even as we move away from the corresponding neutral stability boundary. Inviscidly stable regions (to the right of the black boundary) (1*s*) can succumb to the monotonic instability if $s(\alpha_1 - \beta) < -s$, or (2*s*) will

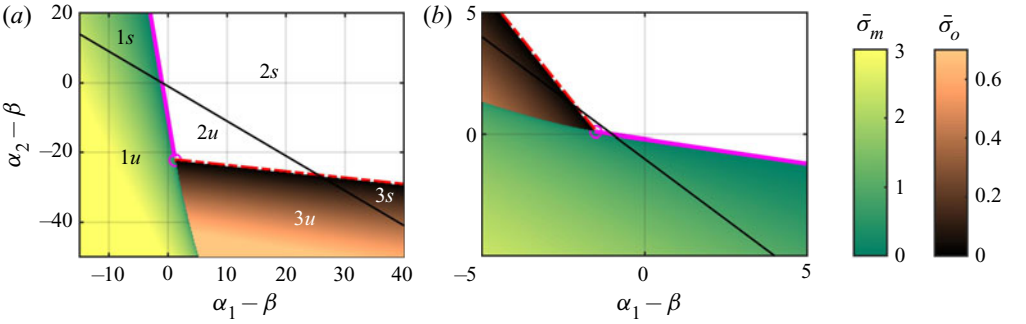

Figure 9. Neutral stability boundaries (3.22)–(3.23) on the $((\alpha_1 - \beta), (\alpha_2 - \beta))$ plane for (a) $Sc = 0.1$, (b) $Sc = 5$. The magenta solid lines separate the stable region from the monotonic instability region (growth rate $\bar{\sigma}_m$ shown using the green colour map). The red dashed lines separate the stable region from the oscillatory instability region (growth rate $\bar{\sigma}_o$ shown using the brown colour map). In both the plots, the magenta circle denotes the location where the neutral stability boundary switches from monotonic to oscillatory instability, and the black line denotes the neutral stability boundary for $Sc = 1$. In (a), labels $(1s, 2s, 3s)$ correspond to inviscidly stable regions and $(1u, 2u, 3u)$ correspond to inviscidly unstable regions.

remain stable if $-s < (\alpha_1 - \beta) < s(Sc^2 + 3Sc + 1)/(Sc(1 - Sc))$, or $(3s)$ can succumb to the oscillatory instability if $s(\alpha_1 - \beta) > s(Sc^2 + 3Sc + 1)/(Sc(1 - Sc))$. In the inviscidly unstable regions, we observe qualitatively three different behaviours: $(1u)$ monotonic instability only, $(2u)$ both monotonic and oscillatory instabilities being absent and $(3u)$ oscillatory instability only. The stable triangular region (region $2u$) is bounded by $[\alpha_1 - \beta, \alpha_2 - \beta] = [-1, 0], [(Sc^2 + 3Sc + 1)/(Sc(1 - Sc)), (4Sc + 1)/(Sc(Sc - 1))], [(1 + Sc)/(1 - Sc), 2/(Sc(Sc - 1))]$. The equation describing the boundary between regions $(1u)$ and $(3u)$ is derived in Appendix C (see (C5)).

In summary of this section, we identified new parameters $(\alpha_1 - \beta, \alpha_2 - \beta, Sc)$ based on an alternate non-dimensionalization, which allowed us to derive analytical expressions for various instability characteristics. Specifically, expressions for the neutral stability boundaries and the interface between monotonic and oscillatory instabilities on the $((\alpha_1 - \beta), (\alpha_2 - \beta))$ plane were derived; in addition, it was also shown that monotonic and oscillatory instabilities cannot simultaneously occur for the same values of the parameters. It is, however, noteworthy that the parameters α_1, α_2 and β are a combination of base flow and perturbation characteristics. The instability characteristics in terms of physically more relevant parameters, which also separate the effects of base flow and perturbations, were earlier presented in §§ 3.2–3.3.

4. Discussion

In this section, we address two different goals, namely (i) to highlight the effects of curvature, an aspect that is relatively less understood, and (ii) to explore typical oceanic regimes and comment on the possibility of the instabilities discussed in § 3.

4.1. *Effects of curvature*

As shown in § 3.3.3, the neutral stability boundaries for the monotonic and oscillatory instabilities are given by (3.18) and (3.19), respectively. In the absence of curvature effects, the neutral stability boundaries are obtained by replacing Γ and Θ by Γ_M and Θ_M, where Γ_M and Θ_M are as defined in (3.6*a*,*b*). We recall that the subscript M refers to the variables

defined in the study of McIntyre (1970), which did not account for curvature effects (see § 3.1); (Γ_M, Θ_M) are related to (Γ, Θ) by

$$\tan\Gamma_M = \tan\Gamma(1+R_c), \quad \tan\Theta_M = \tan\Theta, \tag{4.1a,b}$$

where $R_c = (V/r)/(\partial V/\partial r + 2\Omega)$ is a non-dimensional parameter that quantifies the curvature effects. The unstable region (on the $(Sc, (\tan\Theta_M/\tan\Gamma_M))$ plane) corresponding to monotonic instability (3.18) can now be written in terms of $\tan\Gamma_M$, $\tan\Theta_M$ and R_c as

$$\frac{\tan\Theta_M(1+R_c)}{\tan\Gamma_M} < \frac{(1+Sc)^2}{4Sc}. \tag{4.2}$$

Correspondingly, the unstable region for oscillatory instability (3.19) can be written as

$$\left.\begin{aligned} 0 < \frac{\tan\Theta_M(1+R_c)}{\tan\Gamma_M} &< \frac{(3Sc+1)^2}{8Sc(Sc+1)}, \quad \text{if } Sc<1 \\ \frac{\tan\Theta_M(1+R_c)}{\tan\Gamma_M} &< \frac{(3Sc+1)^2}{8Sc(Sc+1)}, \quad \text{if } Sc>1. \end{aligned}\right\} \tag{4.3}$$

Setting $R_c = 0$ in (4.2)–(4.3) recovers the limit of zero curvature exactly. For $R_c \to \infty$, the unstable regions asymptotically approach $\tan\Theta_M/\tan\Gamma_M < 0$ for monotonic instability at all Sc and oscillatory instability for $Sc > 1$; oscillatory instability does not occur for $Sc < 1$ at $R_c = \infty$. For $R_c \to -\infty$, the unstable regions asymptotically approach $\tan\Theta_M/\tan\Gamma_M > 0$ for monotonic instability at all Sc and oscillatory instability for $Sc > 1$; oscillatory instability again does not occur for $Sc < 1$ at $R_c = -\infty$. In other words, for strongly negative R_c, ignoring the curvature effects can result in qualitatively and quantitatively misleading conclusions in terms of which regions on the $(Sc, (\tan\Gamma_M/\tan\Theta_M))$ plane are unstable. Such misleading conclusions are a result of a change in the sign of $(1+R_c)$ at $R_c = -1$. To quantitatively visualize the effects of curvature, we proceed to plot the neutral stability boundaries on the $(Sc, (\tan\Theta_M/\tan\Gamma_M))$ plane for various values of R_c.

Figure 10 shows the neutral stability boundaries on the plane of Sc and $\tan\Theta_M/\tan\Gamma_M$ for different values of R_c. While the region below the boundaries is unstable for $R_c > -1$, the region above the corresponding neutral stability boundary is unstable for $R_c < -1$. In addition, for all R_c, there is a neutral stability boundary for oscillatory instability at $\tan\Theta_M/\tan\Gamma_M = 0$ for $Sc < 1$ in figure 10(*b*). In the absence of curvature effects, i.e. $R_c = 0$, the black neutral stability boundaries in figure 10(*a*,*b*) are exact. For $R_c \neq 0$, the neutral stability boundaries move away from the black boundaries; however, a theory that ignores curvature effects (McIntyre (1970), for example) always predicts the black boundaries as the neutral stability boundaries. For $R_c > 0$ (red boundaries), the regions of both monotonic and oscillatory instabilities are smaller than what a theory with no curvature effects would predict. On the other hand, for $-1 < R_c < 0$ (blue boundaries), the actual regions of instability are larger than at $R_c = 0$. For a given $R_c > -1$, the distance between the exact and the curvature-effect-free neutral stability boundaries increases as Sc moves away from unity. For $R_c < -1$, the regions of instability are above the corresponding neutral stability boundaries (shown in green for $R_c = -2$), which now lie in the negative half of the plane. Therefore, as mentioned earlier, a curvature-free theory would be completely misleading if $R_c < -1$.

4.2. *Relevant ocean regimes*

In this subsection, we discuss representative ocean regimes to explore the likelihood of occurrence of the instabilities described in this study. As shown in figure 8(*a*), the values of

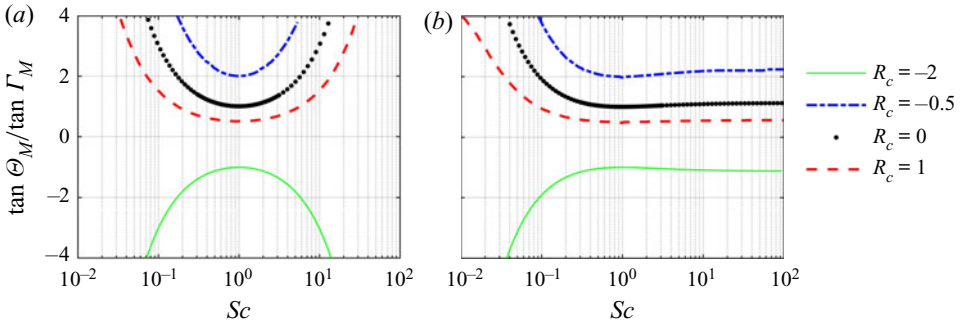

Figure 10. Neutral stability boundaries on the (Sc, (tan Θ_M/ tan Γ_M)) plane (see (3.6*a*,*b*) for the definitions of tan Θ_M and tan Γ_M) for (*a*) monotonic instability (4.2), and (*b*) oscillatory instability (4.3). The green, blue, black and red colours correspond to $R_c = -2, -0.5, 0, 1$, respectively, where R_c is as defined in (4.1*a*,*b*).

Sc and tan Θ/ tan Γ determine if an eddy is susceptible to any short-wavelength instability, be it inviscid or due to differential diffusion between momentum and mass. With respect to Sc, molecular diffusion gives $Sc \approx 7$ for temperature in water, and $Sc \approx 700$ for salinity in water. In highly turbulent flows, the effective diffusion rates for momentum and scalar fields are often assumed to be nearly equal, resulting in a turbulent Schmidt number value near unity (Kays & Crawford 1993; Kays 1994). The turbulent Schmidt number being close to unity, however, is not necessarily valid in stably stratified turbulent flows, as highlighted by numerical simulations (Venayagamoorthy & Stretch 2010) and field data (Salehipour *et al.* 2016). Specifically, Sc can vary from around 0.7 at small Richardson numbers, to around 20 at large Richardson numbers (Elliott & Venayagamoorthy 2011). In addition, the buoyancy Reynolds number also plays a role in determining the value of turbulent Sc (Salehipour & Peltier 2015).

Based on the definition in (3.3), Θ can be physically interpreted as the orientation of isopycnals with respect to the vertical direction. Therefore, its value can range from being very small at front locations (steep isopycnals) to being very large far from fronts (horizontal isopycnals). As a consequence, the magnitude of tan Θ/ tan Γ is close to zero at sharp fronts, and is infinitely large when horizontal stratification is not present, i.e. far from the fronts. Further, in a stable stratification ($N_z^2 > 0$), the sign of tan Θ/ tan Γ would be the same as the sign of Φ. Given the possibility of tan Θ/ tan Γ taking any value in $(-\infty, \infty)$, it is important to accurately estimate the effective Sc in various settings. As noted in figure 8(*a*), the departure of Sc from unity can both increase the range of unstable tan Θ/ tan Γ and introduce the possibility of oscillatory instability.

It is also worthwhile to discuss the importance of curvature effects in various oceanic settings. In mesoscale eddies, for example, the current speed and radius are, respectively, of the order of 1 m s^{-1} and 100 km. These values give estimates for V/r and $\partial V/\partial r$ as 10^{-5} s^{-1}. For cyclonic eddies, as the latitude varies from 0 (equator) to 90° (poles), the curvature parameter in (4.1*a*,*b*) varies from 1 to 0.064. Correspondingly, for anticyclonic eddies, it varies from 1 at the equator to ∞ at a latitude of around 4°N, and then becomes strongly negative slightly northward; R_c then reaches a value of -1 at around 8°N, before asymptotically increasing towards -0.074 at 90°N. The latitude at which R_c reverses sign will be larger for stronger current speeds or smaller eddies. As shown in figure 10, R_c can significantly affect the stability criterion, and a curvature-effect-free theory would therefore be error prone.

Another feature of importance in sub-mesoscale oceanic eddies is their finite extent in both the horizontal and vertical directions. Specifically, intra-thermocline eddies tend to be around 10–20 km and 200–600 m in horizontal and vertical extents, respectively (Nguyen *et al.* 2012), and are often modelled as pancake vortices. Depending on the vorticity distribution, Reynolds number, Froude number, Burger number and Schmidt number, these pancake vortices can be in different instability regimes, including barotropic and baroclinic instabilities (Yim *et al.* 2016; Storer, Poulin & Ménesguen 2018), short-wavelength instabilities such as symmetric and double-diffusive instabilities (Negretti & Billant 2013; Yim & Billant 2016). Some of these instabilities are recognized as driving mechanisms for density layering observed in oceanic eddies (Hua *et al.* 2013). Of specific relevance to our study are the results of Yim & Billant (2016), who performed global stability analysis to investigate short-wavelength and other instabilities in Gaussian pancake vortices. Yim & Billant (2016) also presented results for $Sc \neq 1$, to show that oscillatory instability (McIntyre 1970) occurs at $Sc = 700$ but not at $Sc = 7$. To recall from our results (figure 8), for $Sc > 1$, the entire centrifugally unstable regime is conducive to the oscillatory instability as well; the Gaussian pancake vortex, however, contains centrifugally stable and unstable regions. It would therefore be insightful to evaluate the local stability criteria (and identify the most unstable perturbations corresponding to monotonic and oscillatory instabilities) on all the streamlines in the Gaussian pancake vortex considered by Yim & Billant (2016), to subsequently establish a relation between the local and global stability results.

5. Conclusions

In this study, we performed a local stability analysis of a stratified, axisymmetric vortex in thermal wind balance, which represents a model for large-scale vortices in the ocean and atmosphere. The results are also relevant for fronts that appear in the vicinity of eddies. Using the local stability approach, which is alternate to the conventional normal mode approach of McIntyre (1970), our results extend those of McIntyre (1970) to include both curvature effects and centrifugally unstable regimes. In addition, the limit of small but finite viscous effects are easily recovered with the non-dimensionalization used in our study; this allowed us to explore the entire plane of perturbation characteristics at base flow conditions that were far from the neutral stability boundaries. The local stability framework was first shown to recover the well-known symmetric instability in the inviscid limit (§ 3.2). The study then focused on the effects of Schmidt number, which represents the ratio between momentum and mass diffusivities.

In the viscous, double-diffusive regime, the instability characteristics were shown to depend on five non-dimensional parameters: two base flow parameters, two perturbation parameters and Sc (§ 3.3). Two different instabilities, monotonic and oscillatory, were shown to occur for $Sc \neq 1$. Monotonic instability, which is the same as symmetric instability at $Sc = 1$, can occur for inviscidly stable (absence of symmetric instability) parameter values if $Sc \neq 1$; correspondingly, inviscidly unstable parameter values can become stable for $Sc \neq 1$. Oscillatory instability, characterized by a non-zero imaginary part in the growth rate, occurs only for $Sc \neq 1$. The modification of monotonic and oscillatory instability regimes due to $Sc \neq 1$ were then discussed in detail in the entire parameter space, including the centrifugally unstable regime (§§ 3.3.1–3.3.2). For a given base flow and Sc, the monotonic instability dominates the oscillatory instability in terms of the growth rate, although both instabilities cannot occur simultaneously for the same perturbations. Neutral stability boundaries on the plane of Sc and a modified gradient Richardson number ($\tan\Theta/\tan\Gamma$) were then identified for both monotonic and oscillatory

instabilities (§ 3.3.3). The monotonic instability was shown to significantly extend into the $\tan\Theta/\tan\Gamma > 1$ region when Sc moves away from unity (for both $Sc < 1$ and $Sc > 1$). The oscillatory instability, which does not occur at $Sc = 1$, was shown to occupy a significant portion of the monotonically unstable region in $\tan\Theta/\tan\Gamma > 0$ for $Sc < 1$. For $Sc > 1$, oscillatory instability extends into the entirety of inviscidly unstable ($-\infty < \tan\Theta/\tan\Gamma < 1$) region, with a small excursion to the $\tan\Theta/\tan\Gamma > 1$ region.

In § 3.4, it was shown that it is possible to further reduce the number of governing non-dimensional parameters to three by choosing an alternate non-dimensionalization of (3.1), albeit at the cost of not separating the base flow and perturbation characteristics (§ 3.4). Each of the two newly identified parameters other than Sc represent a combination of base flow and perturbation characteristics. Neutral stability boundaries for both monotonic and oscillatory instabilities were then analytically derived in terms of the aforementioned three parameters. Additionally, it was also shown that monotonic and oscillatory instabilities cannot simultaneously occur for the same values of the parameters. Finally, in §§ 4.1–4.2, the implications of our overall results were discussed from two different view points. Specifically, the curvature effects were quantified in terms of a non-dimensional parameter, and it was shown that ignoring curvature effects can be misleading in typical oceanic settings. In addition to curvature effects, non-traditional effects (inclusion of the complete Coriolis force, Gerkema *et al.* 2008) could also be important, especially near the equator. Indeed, recent studies have shown that the horizontal component of background rotation can significantly affect the symmetric instability (Itano & Maruyama 2009; Kloosterziel, Carnevale & Orlandi 2017; Zeitlin 2018).

In the future, it would be worthwhile investigating the manifestation of the instabilities discussed in this paper in direct numerical simulations, including the nonlinear flow states that would result from these instabilities. To explore short-wavelength instability regimes in realistic oceanic settings, the instability criteria derived in this study could be evaluated in field data (*in situ* and satellite measurements). The results in this study are also potentially useful in interpreting outputs from large-scale climate models, which often use some constant Sc value, unity or otherwise (Danabasoglu *et al.* 2012). An interesting follow-up to this study would be to investigate the effects of non-isotropic diffusivity, which is often the case in stratified oceanic settings, and triple-diffusive effects resulting from the different diffusivities of momentum, temperature and salinity. Finally, while the current study focused on short-wavelength instabilities, other instabilities such as Kelvin–Helmholtz and baroclinic instabilities have to be considered too to construct an overall instability regimes diagram.

Acknowledgements. The authors would like to thank A. Tandon for his input, and B. Fox-Kemper for pointing us to some of the recent literature.

Funding. The authors also acknowledge the Monsoon Mission Grant MM/2014/IND-002, the FIST grant SR/FST/ET-II/2017/109 and the IIT Madras research initiative titled Geophysical Flows Lab.

Declaration of interests. The authors report no conflict of interest.

Author ORCIDs.
Manikandan Mathur https://orcid.org/0000-0002-2133-3889.

Appendix A. Classical double-diffusive instability (salt fingering)

In this appendix, we show that the local stability framework recovers the classical salt fingering instability using a $O(\delta^2)$ scaling for the temperature, salinity and momentum

diffusivities. For a quiescent base flow ($U_B = 0$) with a salinity profile $S_B(z)$ and a temperature profile $T_B(z)$, the local stability equations can be written as

$$\frac{\mathrm{d}\boldsymbol{a}}{\mathrm{d}t} = -b\hat{e}_z + b\boldsymbol{k}\frac{k_z}{|\boldsymbol{k}|^2} - c_\nu|\boldsymbol{k}|^2\boldsymbol{a}, \tag{A1}$$

$$\frac{\mathrm{d}s}{\mathrm{d}t} = -\boldsymbol{a}\cdot\boldsymbol{\nabla}S_B - c_s|\boldsymbol{k}|^2 s, \tag{A2}$$

$$\frac{\mathrm{d}\tau}{\mathrm{d}t} = -\boldsymbol{a}\cdot\boldsymbol{\nabla}T_B - c_\tau|\boldsymbol{k}|^2\tau, \tag{A3}$$

where s, τ denote the leading-order perturbation amplitudes in salinity and temperature, respectively (salinity and temperature perturbations are written as a series similar to (2.10)–(2.12)). The diffusivities of momentum, salinity and temperature are given by $\nu = c_\nu\delta^2$, $\kappa_s = c_s\delta^2$ and $\kappa_\tau = c_\tau\delta^2$, where c_ν, c_s and c_τ are constants. Here, b refers to the leading-order buoyancy perturbation amplitude

$$b = g[\beta s - \alpha\tau], \tag{A4}$$

where β, α are expansion coefficients in salinity and temperature, respectively. Writing (A1) in component form, and substituting (A4), (A1)–(A3) become

$$\frac{\mathrm{d}a_x}{\mathrm{d}t} = (\beta s - \alpha\tau)g\frac{k_x k_z}{|\boldsymbol{k}|^2} - c_\nu|\boldsymbol{k}|^2 a_x, \tag{A5}$$

$$\frac{\mathrm{d}a_y}{\mathrm{d}t} = (\beta s - \alpha\tau)g\frac{k_y k_z}{|\boldsymbol{k}|^2} - c_\nu|\boldsymbol{k}|^2 a_y, \tag{A6}$$

$$\frac{\mathrm{d}a_z}{\mathrm{d}t} = -(\beta s - \alpha\tau)g + (\beta s - \alpha\tau)g\frac{k_z^2}{|\boldsymbol{k}|^2} - c_\nu|\boldsymbol{k}|^2 a_z, \tag{A7}$$

$$\frac{\mathrm{d}s}{\mathrm{d}t} = -a_z\frac{\mathrm{d}S_B}{\mathrm{d}z} - c_s|\boldsymbol{k}|^2 s, \tag{A8}$$

$$\frac{\mathrm{d}\tau}{\mathrm{d}t} = -a_z\frac{\mathrm{d}T_B}{\mathrm{d}z} - c_\tau|\boldsymbol{k}|^2\tau, \tag{A9}$$

where $\boldsymbol{a} = a_x\hat{e}_x + a_y\hat{e}_y + a_z\hat{e}_z$, and $\boldsymbol{k} = k_x\hat{e}_x + k_y\hat{e}_y + k_z\hat{e}_z$.

For a quiescent base flow, (2.13) suggests that any wave vector remains constant. Thus, (A5)–(A9) are a set of constant coefficient, linear, first-order ordinary differential equations. The non-trivial growth rates λ can then be shown to be governed by

$$\hat{\lambda}^3 + (1 + Pr + Pr_s)\hat{\lambda}^2 + [\hat{T} - \hat{S} + Pr_s + Pr + Pr_s Pr]\hat{\lambda} - \hat{S}Pr + \hat{T} + Pr_s Pr = 0, \tag{A10}$$

where $\hat{\lambda} = \lambda/c_s|\boldsymbol{k}|^2$, $Pr_s = c_\nu/c_s$, $Pr = c_\tau/c_s$, $\hat{S} = \beta g(1 - k_z^2/|\boldsymbol{k}|^2)(\mathrm{d}S_B/\mathrm{d}z)/(c_s^2|\boldsymbol{k}|^4)$, $\hat{T} = \alpha g(1 - k_z^2/|\boldsymbol{k}|^2)(\mathrm{d}T_B/\mathrm{d}z)/(c_s^2|\boldsymbol{k}|^4)$. Equation (A10) is identical to the well-known growth rate equation for double-diffusive salt fingering instability (Turner 1973). In summary, we have shown that the $O(\delta^2)$ scaling for diffusivities in the local stability equations allows us to recover the growth rates associated with the double-diffusive salt fingering instability.

Appendix B. Neutral stability boundaries in terms of (α_1, α_2, β, Sc)

In this appendix, we derive the neutral stability boundaries on the $(\alpha_1 - \beta)$, $(\alpha_2 - \beta)$ plane for various Sc. As shown in (3.20), $\lambda^* = (\lambda + c_\nu|\boldsymbol{k}|^2)/(c_\nu|\boldsymbol{k}|^2)$ is governed by

$$\lambda^{*3} + \left(\frac{1 - Sc}{Sc}\right)\lambda^{*2} + [\alpha_1 + \alpha_2 - 2\beta]\lambda^* + \left(\frac{1 - Sc}{Sc}\right)[\alpha_1 - \beta] = 0, \tag{B1}$$

with the neutral stability boundaries occurring at $\mathrm{Re}(\lambda^*) = 1$. To identify these boundaries, we assume $\lambda^* = 1 + \Delta + \mathrm{i}c$ (Δ, c are real), where Δ is small in the neighbourhood of neutral stability boundaries. Substituting this λ^* in (B1), and ignoring terms that are $O(\Delta^2)$ or higher, we get the imaginary part of the equation as

$$-\mathrm{i}c^3 + 3\mathrm{i}c + 6\mathrm{i}c\Delta + \left(\frac{1}{Sc} - 1\right)2\mathrm{i}c(1 + \Delta) + \mathrm{i}c(\alpha_1 + \alpha_2 - 2\beta) = 0. \tag{B2}$$

Solving (B2) for c, we get

$$c = 0 \text{ or } c^2 = 1 + \frac{2}{Sc} + \alpha_1 + \alpha_2 - 2\beta + 2\Delta\left(2 + \frac{1}{Sc}\right). \tag{B3}$$

For $c = 0$, the real part of (B1) reduces to

$$\frac{\alpha_1 - \beta}{Sc} + \alpha_2 - \beta + \frac{1}{Sc} + \Delta\left[\alpha_1 + \alpha_2 - 2\beta + 1 + \frac{2}{Sc}\right] = 0, \tag{B4}$$

which shows that $\lambda^* = 1$ is a root of (B1) on the line

$$\frac{\alpha_1 - \beta}{Sc} + \alpha_2 - \beta + \frac{1}{Sc} = 0, \tag{B5}$$

if $\alpha_1 + \alpha_2 - 2\beta + 1 + 2/Sc \neq 0$. Furthermore, the line (B5) is a neutral stability boundary only if the other two roots of (B1) are stable on it. The roots of (B1) other than $\lambda_1^* = 1 + \Delta$ are given by

$$\lambda_{2,3}^* = -\frac{1}{2}\left(\frac{1}{Sc} + \Delta\right) \pm \frac{1}{2}\sqrt{\left(\frac{1}{Sc} + \Delta\right)^2 - 4\left(\frac{1 + \Delta}{Sc} + \Delta + \alpha_1 + \alpha_2 - 2\beta\right)}. \tag{B6}$$

The roots $\lambda_{2,3}^*$ are real (with $\Delta = 0$) if

$$s(\alpha_1 - \beta) > s\frac{1}{4Sc(Sc - 1)}, \tag{B7}$$

and stable (less than unity) if

$$s(\alpha_1 - \beta) < s\frac{1 + Sc}{1 - Sc}, \tag{B8}$$

where $s = \mathrm{sgn}(1 - Sc)$. If conditions (B7) and (B8) are satisfied, then the eigenvalue that goes from stable to unstable across the neutral stability boundary in (B5) is real, while the remaining two stable eigenvalues are also real in the neighbourhood of the neutral stability boundary. For $\lambda_1^* = 1$, the other two eigenvalues (B6) are complex on the boundary in (B5) if

$$s(\alpha_1 - \beta) < s\frac{1}{4Sc(Sc - 1)}, \tag{B9}$$

and are always stable since their real part is negative for $\Delta = 0$. In other words, if (B9) is satisfied, the straight line in (B5) is a neutral stability boundary, with the eigenvalue

that goes from stable to unstable across the neutral stability boundary being real and the remaining two stable eigenvalues being complex. In summary, (B5) represents the monotonic (since $c = 0$) neutral stability boundary for either conditions (B7) and (B8) being satisfied or condition (B9) being satisfied.

For the case of $c^2 = 1 + 2/Sc + \alpha_1 + \alpha_2 - 2\beta + 2\Delta(2 + 1/Sc)$ in (B3), the real part of (B1) becomes

$$2(\alpha_1 - \beta) + (\alpha_2 - \beta)\left(1 + \frac{1}{Sc}\right) + 2\left(1 + \frac{2}{Sc} + \frac{1}{Sc^2}\right) = -2\Delta\left(\alpha_1 + \alpha_2 - 2\beta + 5 + \frac{1}{Sc^2} + \frac{6}{Sc}\right), \tag{B10}$$

provided $1 + 2/Sc + \alpha_1 + \alpha_2 - 2\beta + 2\Delta(2 + 1/Sc) > 0$. Thus, the line

$$2(\alpha_1 - \beta) + (\alpha_2 - \beta)\left(1 + \frac{1}{Sc}\right) + 2\left(1 + \frac{2}{Sc} + \frac{1}{Sc^2}\right) = 0 \tag{B11}$$

is a neutral stability boundary with $c^2 > 0$ and $\Delta = 0$ (as the third root $\lambda_3^* = -1 - 1/Sc$ is stable) if

$$s(\alpha_1 - \beta) < s\frac{1 + Sc}{1 - Sc}. \tag{B12}$$

The condition in (B12) is obtained based on the requirement of $c^2 > 0$ on the line in (B11). In summary, (B11) is the oscillatory neutral stability boundary for those $(\alpha_1 - \beta)$ satisfying (B12).

Appendix C. Monotonic–oscillatory instability interface

In this appendix, we derive closed form expressions for the interface between monotonic and oscillatory instabilities within the unstable region on the $(\alpha_1 - \beta)$, $(\alpha_2 - \beta)$ plane (see figure 9). Approaching the interface from the oscillatory instability side, we seek solutions of the form $\lambda^* = (a + \mathrm{i}b)$, $(a - \mathrm{i}b)$, c for (3.20), where a, b and c are all real. Comparing the coefficients of (3.20) and the cubic given by $(\lambda^* - (a + \mathrm{i}b))(\lambda^* - (a - \mathrm{i}b))(\lambda^* - c)$, we get $2a + c = -(1 - Sc)/Sc$. If monotonic and oscillatory instabilities were to occur simultaneously, we require $a > 1$ and $c > 1$. (recall that $\mathrm{Re}(\lambda^*) > 1$ for instability). As a result, Sc has to satisfy $(1 - Sc)/Sc > -3$, which is not possible for $Sc > 0$. Hence, for all real values of α_1, α_2, β and Sc, the monotonic and oscillatory instabilities cannot occur simultaneously.

Now, we seek the interface between monotonic and oscillatory instabilities as the boundary where the unstable roots $a + \mathrm{i}b$ have $b \to 0$ while we approach it from the oscillatory instability side. Upon substituting $\lambda^* = a + \mathrm{i}b$, the real and imaginary parts of (3.20) become

$$a^3 - 3ab^2 + \frac{1 - Sc}{Sc}(a^2 - b^2) + [\alpha_1 + \alpha_2 - 2\beta]a + \frac{1 - Sc}{Sc}(\alpha_1 - \beta) = 0, \tag{C1}$$

$$-\mathrm{i}b^3 + 3a^2\mathrm{i}b + \frac{1 - Sc}{Sc}2\mathrm{i}ab + [\alpha_1 + \alpha_2 - 2\beta]\mathrm{i}b = 0. \tag{C2}$$

Solving for b in (C2), and requiring the $b \neq 0$ solution to tend towards zero gives

$$a_\pm \to -\frac{1 - Sc}{Sc} \pm \sqrt{\frac{(1 - Sc)^2}{9Sc^2} - \frac{\alpha_1 + \alpha_2 - 2\beta}{3}}. \tag{C3}$$

For instability, we require $a > 1$, which can be satisfied only by a_+ in (C3). Requiring $a_+ > 1$ gives

$$\alpha_1 + \alpha_2 - 2\beta < -1 - \frac{2}{Sc}. \tag{C4}$$

Noting that $\alpha_1 + \alpha_2 - 2\beta = -1 - 2/Sc$ intersects the monotonic and oscillatory neutral stability boundaries (3.22)–(3.23) at a common location ($\alpha_1 - \beta = (Sc+1)/(Sc-1)$, $\alpha_2 - \beta = -2/Sc(Sc-1)$), and comparing their slopes, it can be shown that the monotonic–oscillatory instability interface satisfies (C4). The equation describing the monotonic–oscillatory instability interface can then be derived by substituting a_+ in (C1) with $b = 0$ to get

$$\frac{2(1-Sc)^3}{9Sc^3} + \frac{1-Sc}{3Sc}(2(\alpha_1-\beta) + (\alpha_2-\beta)) - \left(\frac{2(1-Sc)^2}{9Sc^2} - \frac{2(\alpha_1+\alpha_2-2\beta)}{3}\right)\sqrt{\frac{(1-Sc)^2}{9Sc^2} - \frac{\alpha_1+\alpha_2-2\beta}{3}} = 0. \tag{C5}$$

Appendix D. Neutral stability boundaries in terms of physical parameters

To derive the neutral stability boundaries on the plane of base flow parameters, we first write $\alpha_1 - \beta$ and $\alpha_2 - \beta$ (§ 3.4) in terms of the physical parameters in (3.4*a*,*b*)–(3.5*a*,*b*)

$$\alpha_1 - \beta = \hat{\Phi}\frac{2\cos^2\theta - \tan\Gamma\sin 2\theta}{\tilde{c}^2}, \quad \alpha_2 - \beta = \hat{\Phi}\frac{\tan\Gamma(2\tan\Theta\sin^2\theta - \sin 2\theta)}{\tilde{c}^2}. \tag{D1a,b}$$

In this appendix, we assume $\hat{\Phi} = 1$, i.e. the centrifugally stable regime.

In the neighbourhood of the monotonic neutral stability boundary on the $(\alpha_1 - \beta)$, $(\alpha_2 - \beta)$ plane, the growth rate Δ is governed by (B4). For given base flow parameters, we first maximize Δ with respect to the perturbation parameters, and then identify the $\Delta = 0$ boundary on the plane of base flow parameters. To maximize Δ with respect to θ, we differentiate (B4) with respect to θ to get

$$\frac{1}{Sc}\left(\frac{\partial\alpha_1}{\partial\theta} - \frac{\partial\beta}{\partial\theta}\right) + \frac{\partial\alpha_2}{\partial\theta} - \frac{\partial\beta}{\partial\theta} + \frac{\partial\Delta}{\partial\theta}\left[\alpha_1 + \alpha_2 - 2\beta + 1 + \frac{2}{Sc}\right] + \Delta\left[\frac{\partial\alpha_1}{\partial\theta} + \frac{\partial\alpha_2}{\partial\theta} - 2\frac{\partial\beta}{\partial\theta}\right] = 0, \tag{D2}$$

and substitute $\partial\Delta/\partial\theta = 0$. Furthermore, $\Delta = 0$ on the neutral stability boundary we are seeking, thus reducing (D2) to

$$\frac{1}{Sc}\left(\frac{\partial\alpha_1}{\partial\theta} - \frac{\partial\beta}{\partial\theta}\right) + \frac{\partial\alpha_2}{\partial\theta} - \frac{\partial\beta}{\partial\theta} = 0. \tag{D3}$$

Substituting the expressions in (D1) in (D3) gives the expression for the most unstable θ for monotonic instability as

$$\tan 2\theta^* = \frac{(Sc+1)\tan\Gamma}{Sc\tan\Theta\tan\Gamma - 1}. \tag{D4}$$

Recalling from § 3.3.1 that $\tilde{c} = 0$ on the neutral stability boundaries in the plane of $(Sc, (\tan\Theta/\tan\Gamma))$ and substituting (D4) in (B5), we obtain the monotonic neutral

stability boundary as

$$\frac{\tan\Theta}{\tan\Gamma} = \frac{(1+Sc)^2}{4Sc}. \tag{D5}$$

In the neighbourhood of the oscillatory neutral stability boundary on the $(\alpha_1-\beta)$, $(\alpha_2-\beta)$ plane, the growth rate Δ is governed by (B10). For given base flow parameters, we first maximize Δ with respect to the perturbation parameters, and then identify the $\Delta=0$ boundary on the plane of base flow parameters. To maximize Δ with respect to θ, we differentiate (B10) with respect to θ to get

$$2\left(\frac{\partial\alpha_1}{\partial\theta}-\frac{\partial\beta}{\partial\theta}\right)+\left(\frac{\partial\alpha_2}{\partial\theta}-\frac{\partial\beta}{\partial\theta}\right)\left(1+\frac{1}{Sc}\right)+2\frac{\partial\Delta}{\partial\theta}\left[\alpha_1+\alpha_2-2\beta+5+\frac{1}{Sc^2}+\frac{6}{Sc}\right]$$
$$+2\Delta\left[\frac{\partial\alpha_1}{\partial\theta}+\frac{\partial\alpha_2}{\partial\theta}-2\frac{\partial\beta}{\partial\theta}\right]=0, \tag{D6}$$

and substitute $\partial\Delta/\partial\theta=0$. Furthermore, $\Delta=0$ on the neutral stability boundary we are seeking, thus reducing (D6) to

$$2\left(\frac{\partial\alpha_1}{\partial\theta}-\frac{\partial\beta}{\partial\theta}\right)+\left(\frac{\partial\alpha_2}{\partial\theta}-\frac{\partial\beta}{\partial\theta}\right)\left(1+\frac{1}{Sc}\right)=0. \tag{D7}$$

Substituting the expressions in (D1) in (D7) gives the expression for the most unstable θ for oscillatory instability as

$$\tan 2\theta_o^* = \frac{3Sc+1}{(1+Sc)\tan\Theta-4Sc\cot\Gamma}. \tag{D8}$$

Recalling from § 3.3.1 that $\tilde{c}=0$ on the neutral stability boundaries in the plane of $(Sc, (\tan\Theta/\tan\Gamma))$ and substituting (D8) in (B11), we obtain the oscillatory neutral stability boundary as

$$\frac{\tan\Theta}{\tan\Gamma} = \frac{(3Sc+1)^2}{8Sc(Sc+1)}. \tag{D9}$$

References

Bachman, S.D., Fox-Kemper, B., Taylor, J.R. & Thomas, L.N. 2017 Parameterization of frontal symmetric instabilities. I: theory for resolved fronts. *Ocean Model.* **109**, 72–95.

Baker, D.J. 1971 Density gradients in a rotating stratified fluid: experimental evidence for a new instability. *Science* **172** (3987), 1029–1031.

Billant, P. & Gallaire, F. 2005 Generalized Rayleigh criterion for non-axisymmetric centrifugal instabilities. *J. Fluid Mech.* **542**, 365–379.

Buckingham, C.E., Gula, J. & Carton, X. 2021*a* The role of curvature in modifying frontal instabilities. Part I: review of theory and presentation of a nondimensional instability criterion. *J. Phys. Oceanogr.* **51** (2), 299–315.

Buckingham, C.E., Gula, J. & Carton, X. 2021*b* The role of curvature in modifying frontal instabilities. Part II: application of the criterion to curved density fronts at low Richardson numbers. *J. Phys. Oceanogr.* **51** (2), 317–341.

Calman, J. 1977 Experiments on high Richardson number instability of a rotating stratified shear flow. *Dyn. Atmos. Oceans* **1** (4), 277–297.

Chandrasekhar, S. 1961 Hydrodynamic and Hydromagnetic Stability, Courier Corporation.

Danabasoglu, G., Bates, S.C., Briegleb, B.P., Jayne, S.R., Jochum, M., Large, W.G., Peacock, S. & Yeager, S.G. 2012 The CCSM4 ocean component. *J. Clim.* **25** (5), 1361–1389.

D'Asaro, E., Lee, C., Rainville, L., Harcourt, R. & Thomas, L. 2011 Enhanced turbulence and energy dissipation at ocean fronts. *Science* **332** (6027), 318–322, https://science.sciencemag.org/content/332/6027/318.full.pdf.

ELLIOTT, Z.A. & VENAYAGAMOORTHY, S.K. 2011 Evaluation of turbulent Prandtl (Schmidt) number parameterizations for stably stratified environmental flows. *Dyn. Atmos. Oceans* **51** (3), 137–150.

EMANUEL, K.A. 1979 Inertial instability and mesoscale convective systems. Part I: linear theory of inertial instability in rotating viscous fluids. *J. Atmos. Sci.* **36** (12), 2425–2449.

EMANUEL, K.A., FANTINI, M. & THORPE, A.J. 1987 Baroclinic instability in an environment of small stability to slantwise moist convection. Part I: two-dimensional models. *J. Atmos. Sci.* **44** (12), 1559–1573.

FOX-KEMPER, B., DANABASOGLU, G., FERRARI, R., GRIFFIES, S.M., HALLBERG, R.W., HOLLAND, M.M., MALTRUD, M.E., PEACOCK, S. & SAMUELS, B.L. 2011 Parameterization of mixed layer eddies. III: implementation and impact in global ocean climate simulations. *Ocean Model.* **39** (1–2), 61–78.

FOX-KEMPER, B., FERRARI, R. & HALLBERG, R. 2008 Parameterization of mixed layer eddies. Part I: theory and diagnosis. *J. Phys. Oceanogr.* **38** (6), 1145–1165.

GERKEMA, T., ZIMMERMAN, J.T.F., MAAS, L.R.M. & VAN HAREN, H. 2008 Geophysical and astrophysical fluid dynamics beyond the traditional approximation. *Rev. Geophys.* **46**, RG2004.

GODEFERD, F.S., CAMBON, C. & LEBLANC, S. 2001 Zonal approach to centrifugal, elliptic and hyperbolic instabilities in stuart vortices with external rotation. *J. Fluid Mech.* **449**, 1–37.

HAINE, T.W.N. & MARSHALL, J. 1998 Gravitational, symmetric, and baroclinic instability of the ocean mixed layer. *J. Phys. Oceanogr.* **28** (4), 634–658.

HOLMES, R.M., THOMAS, L.N., THOMPSON, L. & DARR, D. 2014 Potential vorticity dynamics of tropical instability vortices. *J. Phys. Oceanogr.* **44** (3), 995–1011.

HOSKINS, B.J. 1974 The role of potential vorticity in symmetric stability and instability. *Q. J. R. Meteorol. Soc.* **100** (425), 480–482.

HOSKINS, B.J. & BRETHERTON, F.P. 1972 Atmospheric frontogenesis models: mathematical formulation and solution. *J. Atmos. Sci.* **29** (1), 11–37.

HUA, B.L., MÉNESGUEN, C., LE GENTIL, S., SCHOPP, R., MARSSET, B. & AIKI, H. 2013 Layering and turbulence surrounding an anticyclonic oceanic vortex: in situ observations and quasi-geostrophic numerical simulations. *J. Fluid Mech.* **731**, 418–442.

ITANO, T. & MARUYAMA, K. 2009 Symmetric stability of zonal flow under full-component coriolis force—effect of the horizontal component of the planetary vorticity—. *J. Meteorol. Soc. Jpn.* **87** (4), 747–753.

KAYS, W.M. & CRAWFORD, M.E. 1993 Convective heat and mass transfer. In *Heat Transfer: The Laminar External Boundary Layer*, chap. 10, pp. 159–191. McGraw-Hill.

KAYS, W.M. 1994 Turbulent Prandtl number. Where are we? *Trans. ASME J. Heat Transfer* **116** (2), 284–295.

KIRILLOV, O.N. & MUTABAZI, I. 2017 Short-wavelength local instabilities of a circular Couette flow with radial temperature gradient. *J. Fluid Mech.* **818**, 319–343.

KLOOSTERZIEL, R.C. & CARNEVALE, G.F. 2007 Generalized energetics for inertially stable parallel shear flows. *J. Fluid Mech.* **585**, 117–126.

KLOOSTERZIEL, R.C., CARNEVALE, G.F. & ORLANDI, P. 2017 Equatorial inertial instability with full coriolis force. *J. Fluid Mech.* **825**, 69–108.

KLOOSTERZIEL, R.C. & VAN HEIJST, G.J.F. 1991 An experimental study of unstable barotropic vortices in a rotating fluid. *J. Fluid Mech.* **223**, 1–24.

KUZMINA, N. & ZHURBAS, V. 2000 Effects of double diffusion and turbulence on interleaving at baroclinic oceanic fronts. *J. Phys. Oceanogr.* **30** (12), 3025–3038.

LANDMAN, M.J. & SAFFMAN, P.G. 1987 The three-dimensional instability of strained vortices in a viscous fluid. *Phys. Fluids* **30** (8), 2339–2342.

LE DUC, A. & LEBLANC, S. 1999 A note on Rayleigh stability criterion for compressible flows. *Phys. Fluids* **11** (11), 3563–3566.

LEBLANC, S. 1997 Stability of stagnation points in rotating flows. *Phys. Fluids* **9** (11), 3566–3569.

LIFSCHITZ, A. & HAMEIRI, E. 1991 Local stability conditions in fluid dynamics. *Phys. Fluids* A*: Fluid Dyn.* **3** (11), 2644–2651.

MAHADEVAN, A. 2006 Modeling vertical motion at ocean fronts: are nonhydrostatic effects relevant at submesoscales? *Ocean Model.* **14** (3–4), 222–240.

MAHADEVAN, A. & TANDON, A. 2006 An analysis of mechanisms for submesoscale vertical motion at ocean fronts. *Ocean Model.* **14** (3–4), 241–256.

MATHUR, M., ORTIZ, S., DUBOS, T. & CHOMAZ, J.-M. 2014 Effects of an axial flow on the centrifugal, elliptic and hyperbolic instabilities in Stuart vortices. *J. Fluid Mech.* **758**, 565–585.

MCINTYRE, M.E. 1970 Diffusive destabilisation of the baroclinic circular vortex. *Geophys. Astrophys. Fluid Dyn.* **1** (1–2), 19–57.

MCWILLIAMS, J.C. 1985 Submesoscale, coherent vortices in the ocean. *Rev. Geophys.* **23** (2), 165–182.

MEUNIER, P., MIQUEL, B., LE DIZÈS, S., CHOWDHURY, H. & ALAM, F. 2014 Instabilities around a rotating ellipsoid in a stratified rotating flow. In *19th Australasian Fluid Mechanics Conference, Melbourne, Australia* (ed. H. Chowdhury & F. Alam). RMIT University.

MIYAZAKI, T. 1993 Elliptical instability in a stably stratified rotating fluid. *Phys. Fluids* A*: Fluid Dyn.* **5** (11), 2702–2709.

MIYAZAKI, T. & FUKUMOTO, Y. 1992 Three-dimensional instability of strained vortices in a stably stratified fluid. *Phys. Fluids* A*: Fluid Dyn.* **4** (11), 2515–2522.

NAGARATHINAM, D., SAMEEN, A. & MATHUR, M. 2015 Centrifugal instability in non-axisymmetric vortices. *J. Fluid Mech.* **769**, 26–45.

NEGRETTI, M.E. & BILLANT, P. 2013 Stability of a gaussian pancake vortex in a stratified fluid. *J. Fluid Mech.* **718**, 457–480.

NGUYEN, H.Y., HUA, B.L., SCHOPP, R. & CARTON, X. 2012 Slow quasigeostrophic unstable modes of a lens vortex in a continuously stratified flow. *Geophys. Astrophys. Fluid Dyn.* **106** (3), 305–319.

OOYAMA, K. 1966 On the stability of the baroclinic circular vortex: a sufficient criterion for instability. *J. Atmos. Sci.* **23** (1), 43–53.

PEDLOSKY, J. 1987 *Geophysical Fluid Dynamics*, vol. 710. Springer.

PELTIER, W.R. & CAULFIELD, C.P. 2003 Mixing efficiency in stratified shear flows. *Annu. Rev. Fluid Mech.* **35** (1), 135–167.

PIERREHUMBERT, R.T. & SWANSON, K.L. 1995 Baroclinic instability. *Annu. Rev. Fluid Mech.* **27** (1), 419–467.

RUDDICK, B. 1992 Intrusive mixing in a mediterranean salt lens—intrusion slopes and dynamical mechanisms. *J. Phys. Oceanogr.* **22** (11), 1274–1285.

SALEHIPOUR, H. & PELTIER, W.R. 2015 Diapycnal diffusivity, turbulent Prandtl number and mixing efficiency in Boussinesq stratified turbulence. *J. Fluid Mech.* **775**, 464–500.

SALEHIPOUR, H., PELTIER, W.R., WHALEN, C.B. & MACKINNON, J.A. 2016 A new characterization of the turbulent diapycnal diffusivities of mass and momentum in the ocean. *Geophys. Res. Lett.* **43** (7), 3370–3379.

SARKAR, S., PHAM, H.T., RAMACHANDRAN, S., NASH, J.D., TANDON, A., BUCKLEY, J., LOTLIKER, A.A. & OMAND, M.M. 2016 The interplay between submesoscale instabilities and turbulence in the surface layer of the bay of bengal. *Oceanography* **29** (2), 146–157.

SHAKESPEARE, C.J. 2016 Curved density fronts: cyclogeostrophic adjustment and frontogenesis. *J. Phys. Oceanogr.* **46** (10), 3193–3207.

SHCHERBINA, A.Y., *et al.*2015 The latmix summer campaign: submesoscale stirring in the upper ocean. *Bull. Am. Meteorol. Soc.* **96** (8), 1257–1279.

SINGH, S. & MATHUR, M. 2019 Effects of Schmidt number on the short-wavelength instabilities in stratified vortices. *J. Fluid Mech.* **867**, 765–803.

SIPP, D. & JACQUIN, L. 2000 Three-dimensional centrifugal-type instabilities of two-dimensional flows in rotating systems. *Phys. Fluids* **12** (7), 1740–1748.

SOLBERG, M. 1936 Le mouvement d'inertie de l'atmosphere stable et son role dans le theorie des cyclones. In *Meteor. Assoc. U.G.G.I.*, pp. 66–82. Dupont.

STORER, B.A., POULIN, F.J. & MÉNESGUEN, C. 2018 The dynamics of quasigeostrophic lens-shaped vortices. *J. Phys. Oceanogr.* **48** (4), 937–957.

THOMAS, L.N., TANDON, A. & MAHADEVAN, A. 2008 Submesoscale processes and dynamics. *Ocean Model. Eddying Regime* **177**, 17–38.

THOMAS, L.N., TAYLOR, J.R., FERRARI, R. & JOYCE, T.M. 2013 Symmetric instability in the gulf stream. *Deep Sea Res. Part II: Top. Stud. Oceanogr.* **91**, 96–110.

THOMPSON, A.F., LAZAR, A., BUCKINGHAM, C., GARABATO, A.C.N., DAMERELL, G.M. & HEYWOOD, K.J. 2016 Open-ocean submesoscale motions: a full seasonal cycle of mixed layer instabilities from gliders. *J. Phys. Oceanogr.* **46** (4), 1285–1307.

TURNER, J.S. 1973 *Double-Diffusive Convection*, pp. 251–287. Cambridge University Press.

VALLIS, G.K. 2017 *Atmospheric and Oceanic Fluid Dynamics*. Cambridge University Press.

VENAYAGAMOORTHY, S.K. & STRETCH, D.D. 2010 On the turbulent Prandtl number in homogeneous stably stratified turbulence. *J. Fluid Mech.* **644**, 359.

WEBER, J.E. 1980 Symmetric instability of stratified geostrophic flow. *Tellus* **32** (2), 176–185.

XUI, Q. & CLARK, J.H.E. 1985 The nature of symmetric instability and its similarity to convective and inertial instability. *J. Atmos. Sci.* **42** (24), 2880–2883.

YIM, E. & BILLANT, P. 2016 Analogies and differences between the stability of an isolated pancake vortex and a columnar vortex in stratified fluid. *J. Fluid Mech.* **796**, 732–766.

YIM, E., BILLANT, P. & MÉNESGUEN, C. 2016 Stability of an isolated pancake vortex in continuously stratified-rotating fluids. *J. Fluid Mech.* **801**, 508–553.

ZEITLIN, V. 2018 Symmetric instability drastically changes upon inclusion of the full coriolis force. *Phys. Fluids* **30** (6), 061701.

ZHANG, Z., WANG, W. & QIU, B. 2014 Oceanic mass transport by mesoscale eddies. *Science* **345** (6194), 322–324.